INTEGRATION OF ENGINE AND TWC MODELS THROUGH DEVELOPING AN EXHAUST MANIFOLD MODEL FOR PREDICTING MOTOR VEHICLE EMISSIONS DURING DRIVE CYCLES

A Thesis

by

OSAMA DESOUKY

Submitted to the Graduate and Professional School of
Texas A&M University
in partial fulfillment of the requirements for the degree of

MASTER OF SCIENCE

Chair of Committee, Nimir ElBashir
Co-Chair of Committee, Reza Tafreshi
Committee Members, Ioannis Economou

Head of Department, Victor Ugaz

May 2022

Major Subject: Chemical Engineering

ABSTRACT

Estimating emissions of an internal combustion engine depends on the interactions between different vehicle components, such as the three-way catalyst (TWC) and the exhaust manifold. This thesis focuses on developing a transient integrated low-order model for multi-cylinder spark-ignition engines to predict the formation, transfer, and reduction of significant pollutants NO, CO, CO_2, O_2, and UHC (unburned hydrocarbons). This was achieved through integrating four models: a torque-speed model, an exhaust manifold model, a combustion model, and a TWC model.

The combustion process is modeled as a continuously stirred-tank reactor (CSTR) and assumes a simplified gasoline formulation using a two-lumped reaction mode. The exhaust manifold is modeled based on the conservation of energy, mass, and momentum equations and presented by a set of three first-order hyperbolic partial differential equations (PDEs). The exhaust gas properties at the manifold are obtained by using the Lax-Wendorff numerical scheme to solve the PDEs. The gas velocity, temperature, and density are estimated throughout the manifold length and operating times. The emission reduction in TWC is predicted by a lumped analysis of reductants and oxidants and accounts for oxygen. It is assumed that the reaction only occurs at the wash coat, and symmetry simplifies the TWC from a three-dimensional to one-dimension model.

The integrated model is coupled with a torque-speed model to convert a predefined vehicle speed profile to the engine's torque and RPM by considering the main powertrain components: flywheel, gearbox, differential drive-axle, and wheel size. The

emission prediction with the torque-speed model minimizes extensive emission mapping techniques and optimizes the various vehicle system dependencies

The variations between experimental data and theoretical models are mainly due to their difference in spark timing, fuel composition, heating value, and the exact molecular weight of fuel. The fuel data is imported from literature, where quantifying fuel composition accurately would improve the model's prediction accuracy and improve the overall combined model emissions prediction for SI (spark ignition) engines. The integrated model presented here sites the ground for developing and testing customized driving cycles for future emission regulation purposes.

Keywords

TWC, Combustion, Exhaust manifold, pollutant, emissions, drive cycles

ACKNOWLEDGMENTS

I would like to deeply thank my thesis committee co-chair Dr. Reza Tafreshi, for all the guidance, support, advice, and mentoring. I would like to extend my appreciation to the committee chair, Dr. Nimir ElBashir, and committee member Dr. Ioannis Economou for their feedback and input along with the development of this thesis.

I would also like to thank my friends, colleagues, and university staff for making time to help me and guide me when needed.

I would like to acknowledge Dr. Punkaj K. and Prof. Balakotaiah Vemuri for providing the original codes for the SI model.

Finally, thanks to my family for providing me with moral and emotional support through the hardest times.

CONTRIBUTORS AND FUNDING SOURCES

Funding Sources

This work was made possible by Qatar National Research Fund under Grant Number NPRP-7-829-2-308. Its contents are solely the responsibility of the authors and do not necessarily represent the official views of the Qatar National Research Fund.

NOMECLATURE

AFR	Air Fuel Ratio
CI	Compression Ignition
ECU	Engine Control Unit
EIA	U.S. Energy Information Administration
EPA	Environment Protection Agency
FTP-75	Federal Test Procedure for Light Vehicle Testing
GHG	Green House Gas
HEGO	Heated Exhaust Oxygen Sensor
mpg	miles per gallon
mpg-e	miles per gallon equivalent
NEDC	New European Driving Cycle
Nu	Nusselt Number
Pr	Prandtl Number
Re	Reynold Number
SI	Spark Ignition
TWC	Three-Way Catalyst
UEGO	Universal Exhaust Oxygen Sensor
WLTC	Worldwide Harmonized Light Vehicles Test Cycle
a	Speed of Sound in Air
D	Manifold Diameter
f	Friction Factor

k	Specific Heat Ratio
M	Mass
P	Pressure
q	The Rate of Heat Transfer per Unit Time per Unit Mass of Gas
T	Gas Temperature
t	Time
u	Particle Velocity
X	Distance
A_f	Vehicle Frontal Area
c_d	Drag Coefficient
c_v	Specific Heat Capacity at Constant Volume
F_r	Force Rolling Resistance
F_{gr}	Force Grade-Dependent
F_{tr}	Force Total Traction
F_a	Force Aerodynamic
$G_v \frac{d\omega}{dt}$	Vehicle Acceleration
G_e	Engine Moment of Inertia
G_v	Vehicle Inertia
G_x	Other Vehicle Components Moment of Inertia
i_g	Engaged Ratio of the Gearbox
i_b	Back Axle Ratio

$\dot{m}_{real}$	Mass Flow Rate
m_v	Total Mass of Vehicle
N_A	Wheel rotation Speed
N_c	Clutch Rotation Speed
N_s	Propeller Shaft Speed
N	Engine Rotation speed
P_T	Throttle Pressure
p_o	Reference Pressure
r_{wheel}	Wheel Radius
T_o	Reference Gas Temperature
γ	1.4
$\mathcal{F}$	Area
η_g	Gear Efficiency
ρ	Density
τ_e	Engine Torque
τ_w	Shear Stress at the Wall
τ_{tr}	Traction Torque
ω	Engine Angular Velocity

TABLE OF CONETNTS

Page

LIST OF FIGURES

Page

LIST OF TABLES

Page

1. INTRODUCTION

1.1. **Background**

Motor vehicles impacts on the environment become more noticeable, represented by greenhouse gases, excessive energy uses, and localized pollution in the form of heat and noise. During the 1970s, emission standards were initiated in the US, Europe, and Japan, and by the 1990s, the rest of the world followed a similar approach in formulating and implementing an emission regulatory.

Complying with strict regulations requires highly effective and long-lasting solutions. In 1980, a remarkable improvement in motor vehicle emission control and after-treatment systems were embraced by the use of a catalyst body within the vehicle known as Three-Way Catalyst (TWC), which is a monolith reactor placed across the exhaust gas stream that does not have a significant effect on engine performance. Inside the TWC, nitrogen oxides (NO_x) are reduced to nitrogen (N_2), and carbon monoxide (CO) is oxidized to carbon dioxide (CO_2). Also, under ideal operating conditions, the unburnt hydrocarbons are fully combusted to CO_2 and H_2O.

Along with the progressing regulations, a recent US regulation by the environmental protection agency (EPA) dictates an average fleet fuel economy of 55 mpg (4.27 L/100km) by 2025 [1]. Over the past decades, strict progressive regulations have pushed car manufacturers to improve emission control solutions through the use of TWC, selective catalytic reduction (SCR), and lean NOx traps (LNT). These catalyst bodies have shown to be effective in meeting legal limits while maintaining vehicle performance.

Catalytic emission reduction technologies present a solution in complying with environmental regulations. However, accurate representation and evaluation of the overall emission process are required. Detailed physico-chemical models for combustion and after-treatment systems show good accuracy with real-world vehicle's data. But, these models are computationally extensive and not in line with the need for onboard diagnostics and real-time simulations [2]. Consequently, 1-D fluid dynamic models are widely used to simulate the exhaust gas flow. 1-D modeling and real-time simulations in the automotive research field present a goal due to the complex interactions among various vehicle components such as the engine valves, exhaust manifold, TWC, silencers, and mufflers. Additionally, the TWC performance is unpredictable during cold start and transient operation. These motivations present a need for detailed and updated models for predicting emissions during these stages of vehicle operation.

In addition to emission regulations, a test procedure must be performed for governments to certify any new vehicle. The standard test procedure, known as the driving test cycle, uses a chassis dynamometer and an emission analysis system to measure the tailpipe emissions during specified speed-time variation schemes. For example, FTP-75 in the US federal test procedure for light vehicle testing, NEDC as the new European driving cycle, and WLTC as the worldwide harmonized light vehicle test cycle. The test drive cycles intend to reflect real-world driving by resembling the actual driving conditions in a controlled environment.

1.2. **Environmental Pollution and Regulatory**

The presence of particulate matter (PM) and gaseous pollutants such as CO, CO_2, N_2O, NO_x, and SO_x, and VOC (volatile organic compounds) from the transportation sector exposes communities worldwide to suffer health issues from air pollution and climate change. Figure 1-1 shows a report on CO_2 emissions from transportation sector. It indicates that. Governmental regulations and policies are expected to decline the increasing emissions to 1990 levels by 2050. On a similar note, NO_x emissions from transportation account for approximately 50% of the NO_x produced nationally [3]. NO releases react with ozone to form NO_2, and HNO_2 leading to strokes, hypertension, learning disorders, cancers, and other unidentified diseases.

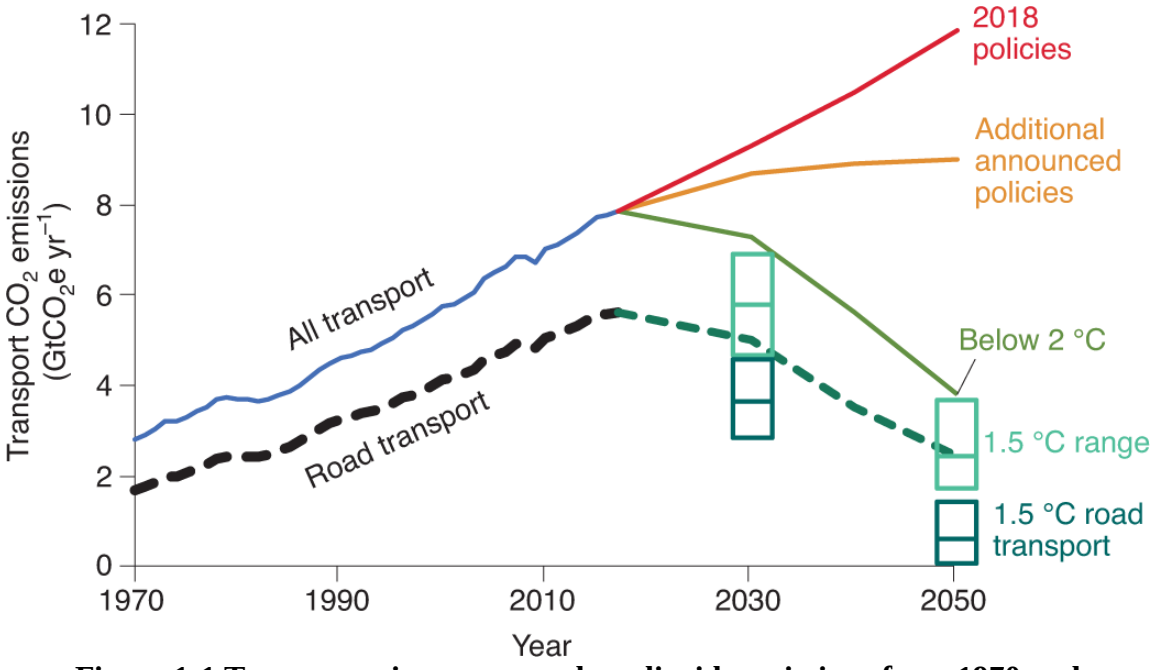

Figure 1-1 Transportation sector carbon dioxide emissions from 1970 and predicted to 2050

Table 1-1 Estimated emission reductions from the Tier 3 standards after 2010

	2018		2030	
	Tons	% of on road inventory	Tons	% of on road inventory
NO_x	264,369	10	328,509	25
VOC	47,504	3	167,591	16
CO	278,879	2	3,458,041	24
Particulate Matter	130	0.1	7,892	10
Benzene	1,916	6	4,762	26
SO_2	14,813	56	12,399	56

EPA Tier 3 standard aims to improve emissions control for both existing and new vehicles. Based on Tier 3 regulatory, Table 1-1 shows the estimated reduction from 2010 to 2030. In line with lowering motor vehicle emissions, EPA greenhouse gas emission (GHG) standards obligate vehicle manufacturers to improve their fuel economy schemes by 2025, resulting in reductions in CO_2 emissions and fuel usage. The EPA anticipates a CO2 fleet average equivalent to 51.4 mpg-equivalent in nowadays' emission data. The actual CO_2 emission performance should not exceed 233g/mi, and the minimum actual fuel economy would be approximately 36 mpg.

1.3. **Objectives**

This study provides an integrated low-order emissions model for vehicle emissions during test cycles, the emissions model represented by three components: (1) engine, (2) exhaust manifold, and (3) TWC of a multi-cylinder SI engine. The comprehensive model developed utilizes an exhaust manifold model based on conservation laws. Based on a continuously stirred tank reactor (CSTR) concept, the engine model estimates the vehicle emissions leaving the cylinder. The model calculates the exhaust gases' temperature, pressure, and velocity as a function of both time and distance along the manifold. The exhaust manifold model helps optimize the location of TWC and consequently minimize cold-start emissions and maximize TWC life span. Besides developing the emissions model, the current study reviews available low-order models to select the proper combustion and TWC sub-models. The overall emission model provides a fast and reliable developing tool for estimating the tailpipe emissions of a multi-cylinder SI engine.

Emissions model performance is evaluated on the FTP-75 cycle. The integrated emission evaluation uses a developed torque-speed sub-model to reflect on engine RPM and loads. The torque-speed sub-model allows testing and simulating the driving cycles, replacing the need for a full-scale chassis dynamometer for evaluation. The torque-speed model converts the vehicle’s speed-time test schemes of the test cycle to engine torque, RPM, load, and inertia as a function of time.

The study is divided into three main milestones:

1- Develop an integrated 1D model of the engine-exhaust-TWC system.

2- Develop a torque-speed model for the vehicle under study.

3- Simulate and implement the FTP-75 cycle for torque and engine speed.

1.4. **Benefits to Industry and Research Fields**

With the increased interest in-vehicle systems simulation, various models have focused on optimizing individual components such as TWC and engine combustion. It is essential to note that interactions between multiple parts play a vital role in achieving a complete representation of emissions. The demands to improve fuel efficiency, lower greenhouse gases, and provide accurate results for engine simulation models have become increasingly desirable. Integrated TWC and engine models offer a variety of tools for engine control design and optimization. Integrating a comprehensive model in programming software such as Matlab can give the user powerful design tools in a single framework. The overall emission model offers the capability of integration with other components such as silencers and LNTs.

The integrated model supports engine developers in reducing emissions and improving fuel economy, reflecting on the environment. The overall model improves prediction accuracy for emission during transient operation, helping optimize the engine operation and improving fuel economy.

1.5. **Thesis Structure**

This thesis is divided into four main chapters:

In Chapter 2, each model used for the comprehensive model is presented in detail. Each sub-section presents a literature review, mathematical model presentation, and the solution method. The Chapter consists of five sub-sections. (1) Combustion and

after-treatment system combination; this section deals with the emission modeling from the engine until after the TWC and illustrates the boundary conditions and limitations of the model. (2) Engine torque-speed for complete system characterization; this sub-section deals with the experimental design and plan for obtaining both steady-state and transient emissions experimentally. (3) Experimental setup and laboratory measurements. (4) Emission collection criteria; this sub-section shows the steps to collect data for validating the models.

The third Chapter presents experimental results for the models. The results focus on (1) exhaust manifold simulation and experimental validation and (2) the torque-speed model results using hypothetical vehicle parameters.

In the fourth and last Chapter, conclusions on the validity and accuracy of the models, followed by future work recommendations to expand the comprehensive model. Appendix A shows a presentation of TWC and combustion models, including kinetic parameters, heat transfer, species balance, energy balance, and fuel composition effect on the model.

2. VEHICLE COMPONENTS MATHEMATICAL MODELS DEVELOPMENT AND VERIFICATIONS

Mathematical modeling of vehicular components has assisted in predicting chemical species conversion through the TWC, LNT (Lean NOx Trap), SCR (Selective Catalytic Reduction), and other vehicle components. This development reduced the need for complicated lab experiments in developing new technologies. The following sub-sections introduce individual models for TWC, combustion, exhaust manifold, and experimental validation criteria.

2.1. **Experimental Setup and Laboratory Measurements**

The developed model validation uses a 3.5 Liter six- cylinder (V6) engine connected to an engine dynamometer. The experimental setup includes multiple measuring ports for exhaust gasses and various pressure and temperature transducers across the exhaust manifold. Figure 2-1 shows a schematic for the experimental setup; emissions measurements use a Horiba MEXA 7071EGR for measuring and analyzing the emissions. The experimental setup uses an AVL Indi microdata acquisition (DAQ) system with integrated encoders and pressure transducers to obtain pressure and temperature at the exhaust manifold. Figures 2-2 and 2-3 show the emissions and pressure transducers locations. While keeping the engine running conditions constant, measurements are quasi-steady from each port in sequence.

The Horiba MEXA7170D EGR equips seven analyzers: CO, CO_2, H_2, THC, O_2, NO, and NO_x. Table 2-1 list technical data for emission bench features. Figure 2-4 shows the Horiba machine and the calibration gases for analyzers.

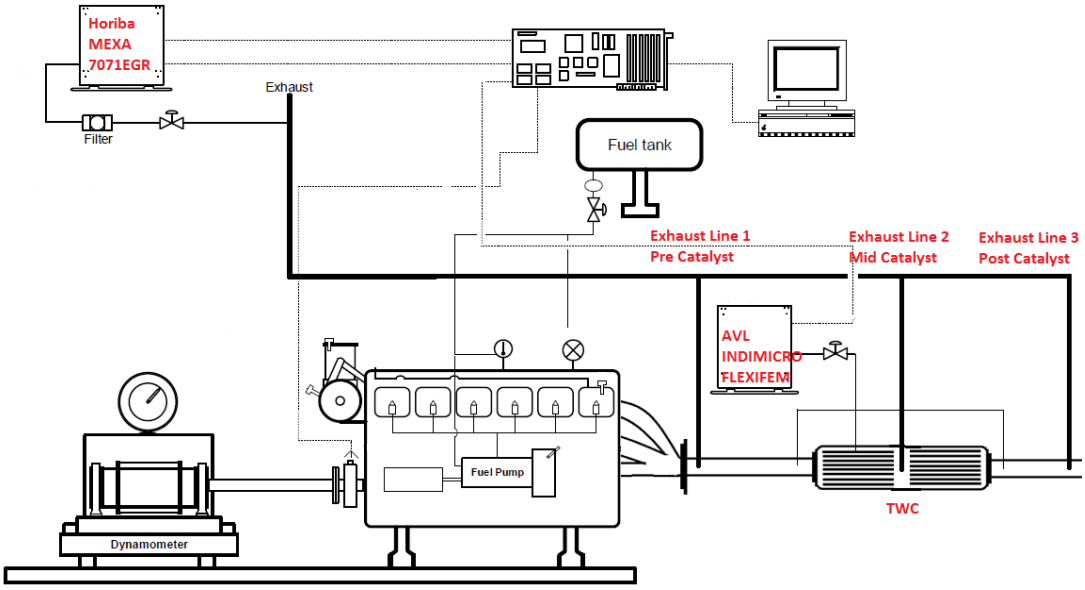

Figure 2-1 Schematic of the experimental setup

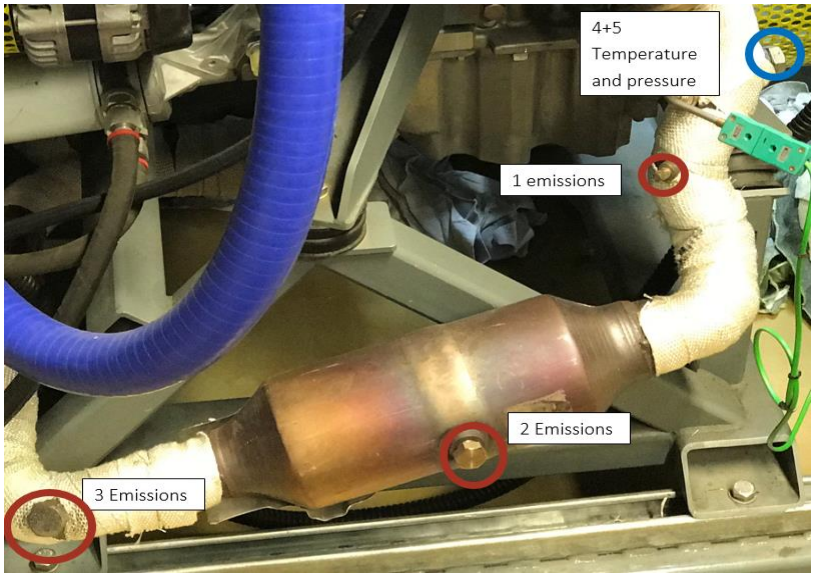

Figure 2-2 Emission sampling locations

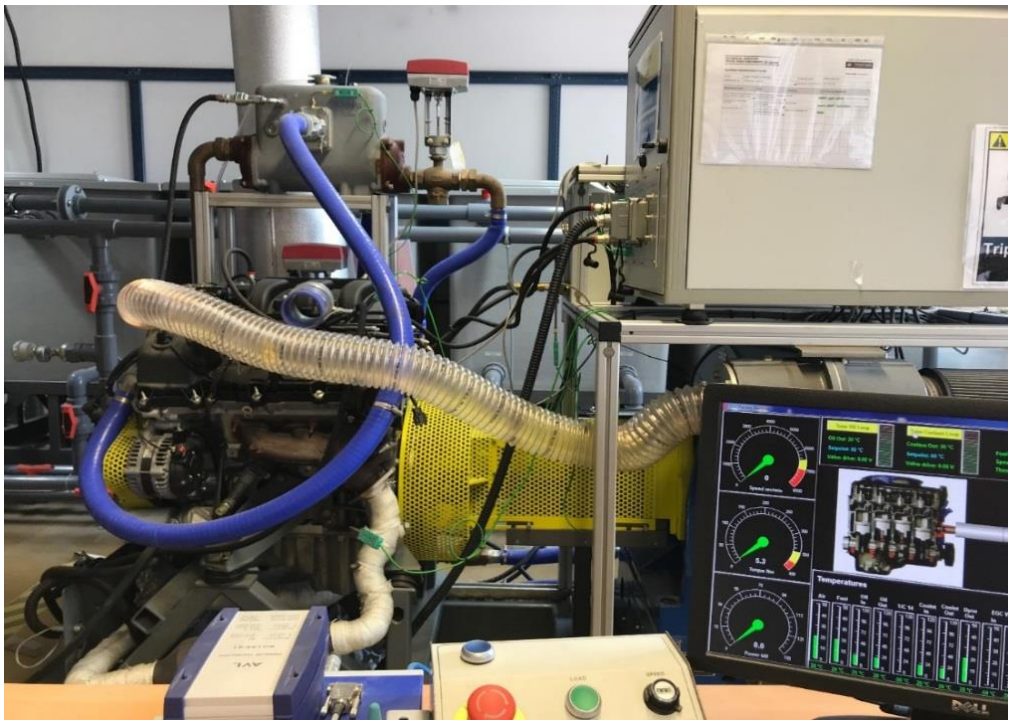

Figure 2-3 Image of the engine used for experimental analysis

Figure 2-4 Emission analytical units setup

Table 2-1 Horiba emission test bench specifications

Sampling points	Raw exhaust gas
Measuring principle CO/CO2	Non-Dispersive Infrared Detector (NDIR)
Range:	CO: 0 – 0,5 ~ 12 Vol.%* (heated) CO_2 : 0 – 0,5 ~ 20 Vol.% *
Measuring principle H/THC	Heated Flame Ionization Detector (FID)
Range (THC):	0 – 10 -500 ppmC (Normalized concentration with respect to calibration gas)
Measuring principle: O2	Magneto-Pneumatic Detector (MPD)
Range O2	0 -1 -25% *.
Measuring principle: NO / NOx	Chemiluminescence Detector (CLD)
Range NO / NOx	0 – 10 ~ 500 ppm

2.2. **Engine Emission Collection Criteria**

Experimental investigation tabulates emissions at engine speed and torque collected at quasi-steady conditions. The Experimental design considers seven rotational speeds for the engine and five load cases; RPM ranges from 1,000 to 4,000 on 500 RPM increments. The engine characterization uses 35 measurement points for the engine conditions. The engine system uses DAQ Factory software to log the experimental data simultaneously at the specified speed and load combination. The sampling rate is one sample per second for:

- Engine Speed
- Torque
- Power
- Fuel flow and temperature
- Airflow and temperature
- Inlet manifold pressure
- Exhaust manifold Temperatures
- Coolant temperature

The exhaust manifold pressure data is collected using the AVL Indicom Microsystem at each crank angle. The data collected are synchronized and averaged to minimize random errors within the system.

2.3. **Exhaust Manifold Model**

The development of an environmentally effective tailpipe emission system lies in predicting the performance of TWC accurately. Developing an exhaust manifold model based on conservation equations helps predict the exhaust gas properties upstream of the TWC and consequently improves the tailpipe emission predictions. The exhaust properties depend on the system's configuration, TWC temperature, and mass flow rates. Exhaust gases from the engine vary in temperature, pressure, and density affecting the performance of the TWC. Accurately predicting the exhaust gas properties such as temperature, pressure, velocity, and density is crucial to the conversion efficiency of TWC.

2.3.1. Background on Exhaust Manifold Modeling

Exhaust manifold models based on first principles use momentum, mass, and energy conservation equations, from which a set of hyperbolic first-order differential equations defines the exhaust manifold. The analytical solution of the conservation

equations is computationally extensive; accordingly, numerical solution schemes deem appropriate in low order modeling of exhaust gases.

Exhaust manifold models are divided based on the entropy assumption; models of entropy generation are known as non-homentropic models. The absence of strong viscous characteristics of exhaust gas that affect the shear stress and frictional losses at the gas-manifold interface simplifies the model to a homentropic (constant entropy) flow relation [4], [5], where the entropy level within each fluid particle is constant with time but a particle-to-particle variation is possible.

The exhaust manifold model is represented by four equations to identify gas properties' velocity, temperature, density, and pressure. These equations are continuity, energy, momentum, and an equation of state.

The homentropic gas assumes minimal deviation of exhaust gas properties with temperature dependent specific heat capacities, the exhaust was simplified as an ideal gas with constant heat capacities for each regulated emissive specie. The general assumption considers the exhaust gas as a mixture of ideal gases with variable specific heats that depend on temperature and chemical composition. However, Benson et al.[4][5] examined a non-steady flow of gases with variable specific heats and showed comparable results with constant specific heat models. Consequently, constant specific heat models for chemical constituents are valid for modeling gas dynamics along the exhaust manifold with less complexity.

The chemical composition of exhaust gases depends on the out-of-cylinder gas composition, assuming pure species transport. The inclusion of conservation equations

allows the estimation of chemical information lengthwise the intake and exhaust manifolds. The engine dynamics of expelling exhaust gases from the cylinder to the manifold resembles a sudden shock at the manifold cylinder interface; consequently, the model uses shock-capturing schemes. Among the conventional methods in gas simulation software are Two-step Lax-Wendorff, McCormack predictor-corrector, conservation element-solution element methods. In addition to conventional methods, higher-order models use flux corrected transport and total variation diminishing algorithms to enhance the prediction accuracy. The finite difference method (FDM) and finite volume methods (FVM) presents higher-order accuracy when compared to the method of characteristics (MOC). A complete review of numerical schemes for solving the unsteady 1D gas dynamics is provided in Winterbone et al. [5]. The following is a summary of selected methods.

Lakshminaryanan et al. [6] used an FDM with a central spatial and explicit Runge-Kutta temporal integration. Takizawa et al. [7] utilized a two-step Lax-Wendroff (LW2) scheme to simulate the exhaust gas exchange process. LW2 presents a first-order accuracy scheme due to artificial viscosity that prevents short-wavelength oscillations. Similarly, Meisner et al. [8] used a MacCormack FDM based on a two-step predictor-corrector approach; Chapman et al. [9] used a filtering remedy and methodology algorithm (FRAM) to calculate the gas dynamics at the exhaust and inlet manifolds. Using FRAM allows optimizing computational effort through using higher-order FDM in parts of the flow where lower-order schemes diverge and cause oscillations. Morel et al. [10] used a staggered mesh based on an FVM approach utilizing quasi-second-order-

donor cell representation. Similarly, Peters et al. [11] introduced an implicit FVM technique using a staggered mesh, a second-order upwind-central scheme, and no iterative PISO algorithm. To rectify the errors presented by shock discontinuities, introducing total variation diminishing (TVD) [12], [13] helps in improving the solution accuracy intermittent gas dynamic problems. The TVD schemes use a similar approach to FRAM. Chakravarthy et al. [14] used a TVD method that compensates between robustness and accuracy tradeoffs through using an explicit FVM with the first-order accuracy in time and a third-order accuracy in space.

Kirkpatrick et al. [15] experimentally validated a 1D model of the unsteady gas flow in engine ducts for both homentropic and non-homentropic MOC and LW2 FDM using flux correction transport (FCT) [13]. Experimental results showed that MOC is less accurate when significant entropy changes are present, as in the case of exhaust gases. On the other hand, most FDM approaches have shown comparable results with experiments. Morel et al. [16] experimentally validated an FVM approach and showed acceptable results. When comparing FDM and FVM, Peters et al. [11] showed that both FDM and FVM could accurately predict the gas properties in engine manifold with accuracy reaching 95%. However, FVM is convenient when studying the conservation of variables, even though both FDM and FVM are similar in accuracy.

Onorati et al. [17] used the MacCormack method to improve accuracy using FCT and TVD schemes to include chemical species transport along the engine ducts. The symmetric conservation element-solution element method shows to be superior in estimating the chemical species transport across the manifolds of the engine. TVD

method introduces excessive diffusion to the numerical solution, which causes data to scatter at discontinuities such as the regions of sudden expansion. On the other hand, FCT cannot fully eliminate the oscillation imposed by first-order methods. Consequently, TVD is preferable to FCT when dealing with contact discontinuities that include chemical species transport.

The gas exchange process is the key to connecting different engine subsystems. Researchers have achieved full system simulation using both detailed and simplified 1D models. For instance, Zhang et al. [18] used Matlab Simulink to integrate the engine combustion model with engine ducts models. Opposing to Morel et al., Zhang et al. [19] use a collocated mesh rather than staggered. This approach increases the model's robustness and allows flexibility in coupling various engine subsystems. The model presentation uses symbolic features of Simulink for model coupling, which enhances the flexibility of the model for parameter changes.

Similarly, Onorati et al. [20] developed a 1-D fluid dynamic program named GASDYN with the capabilities of predicting chemical species transport through vehicle ducts of a single-cylinder engine. The program is capable of representing the exhaust gas backflow during valve overlap. Similar to Benson et al. [21] the gas is assumed to be a mixture of ideal gases with variable specific heats, depending on entropy, chemical composition, and temperature. GASDYN takes a constant pressure model for complete simulation, which was experimentally validated and showed good agreement with simulation results.

2.3.2. Exhaust Manifold Mathematical Model Development

Figure 2-5 depicts a typical exhaust manifold configuration schematic, where gasses pass from the engine block to the TWC. The system consists of the manifold accumulator (point 1 to point 2), where gases accumulate from each cylinder and pass to the takedown pipe (point 2 to point 3), connecting the manifold accumulator to TWC. The manifold serves two principal functions: (1) accumulating gases and (2) dampening high-pressure gas pulses traveling from the cylinder towards the TWC inlet.

Manifold designers aim to improve pressure wave-dampening characteristics at the interface (shown at point 1) and eliminate choking of gases through the manifold to avoid sonic velocities of gases. The evacuation process relies on the inertia forces created by the in-cylinder fast-moving gases, which causes a gas-scavenging phenomenon during the overlap period of the valves.

The exhaust gas flows interconnected with the cylinder and TWC at the interface by setting appropriate boundary conditions at both manifold ends. The model assumes closed-end and open-end boundary conditions at the TWC and cylinder, respectively. At the closed end of the cylinder, initial conditions are set to adapt the in-cylinder exhaust properties such as pressure, velocity, and temperature. In conjunction with boundary conditions, the model includes the physical system parameters such as heat transfer parameters (conduction and convection), friction factors, and geometric corrective factors.

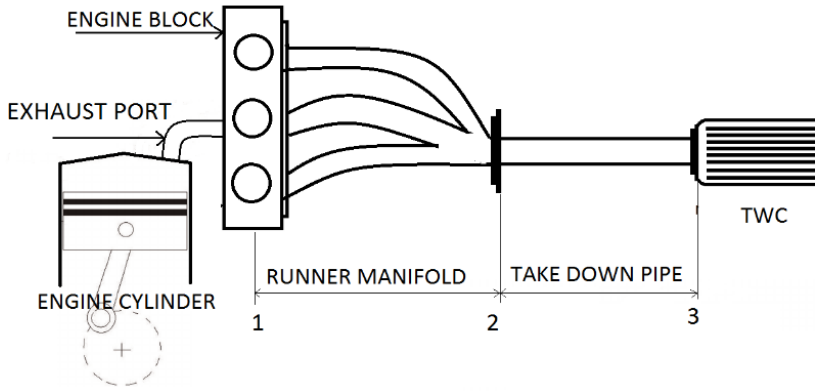

Figure 2-5 Exhaust manifold schematic relating engine-exhaust-TWC

2.3.2.1. Exhaust Manifold Conservation Equations

The exhaust gas flow is approximated as homentropic with constant specific heat. Benson et al. [4] showed that for a non-steady flow, such as exhaust gases, considering the specific heat as a variable in the model increases the problem's complexity without a substantial increase in the accuracy. For the exhaust manifold, the continuity equation is given:

$$\frac{\partial \rho}{\partial t} + \rho \frac{\partial u}{\partial x} + u \frac{\partial \rho}{\partial x} + \frac{\rho u}{\mathcal{F}} \frac{d\mathcal{F}}{dx} = 0, \tag{1}$$

where t is time, x is spatial variation, u is gas velocity and F surface area, ρ is the density. The governing momentum balance is given by:

$$\frac{\partial u}{\partial t} + u \frac{\partial u}{\partial x} + \frac{1}{\rho} \frac{\partial p}{\partial x} + \frac{4f}{D} \frac{u^2}{2} \frac{u}{|u|} = 0, \tag{2}$$

where *p, f,* and *D* represent the manifold pressure, friction factor, and diameter of the manifold. The numerical solution provides the pressure changes in both temporal and spatial variation across the manifold. The friction factor is calculated as:

$$f = \frac{\tau_w}{\frac{1}{2}\rho u^2}, \tag{3}$$

where *f* defines the friction factor of the takedown pipes.

Applying the energy conservation through the first law of thermodynamics, the temporal and spatial variation of temperature, velocity, and density of gas along the exhaust manifold is:

$$q\rho\mathcal{F}dx = \frac{\partial}{\partial t}\left[(\rho\mathcal{F}dx)(c_v T + \frac{u^2}{2})\right] + \frac{\partial}{\partial x}\left[(\rho u\mathcal{F})(c_v T + \frac{p}{\rho} + \frac{u^2}{2})\right]dx, \tag{4}$$

where C_v represents specific heat capacity at constant volume and *q* accounts for the heat transfer rate per unit time per unit mass of fluid transferred by convection through the walls and conduction along the streamlines. By assuming constant specific heat for each specie [22], energy balance for gas in the takedown pipe simplifies to

$$q = mc_p(T_2 - T_1). \tag{5}$$

Combining equations (1) and (2) represent the pulsating behavior of gases:

$$\frac{\partial}{\partial t}(u\rho) + \frac{\partial}{\partial x}(\rho u^2 + p) = -\rho u^2 \frac{d\ln F}{dx} - g\rho \tag{6}$$

For combination and modeling purposes, in the absence of choked flow, the parameters limit to a homentropic flow with constant entropy. For the exhaust gases, the exhaust manifold restricts the flow at the exhaust valve outlet resulting in instability at the manifold inlet. However, the weighted time average is a common technique to overcome

the computational complexity at the restriction [23], [24]. For heat transfer, Sieder-Tate and Gnielinski [25] proposed collating Nusselt's (Nu) number with Reynolds (Re) and Prandtl (Pr) numbers:

$$Nu = \frac{\frac{f}{8} Re.Pr}{1.07 + 12.7\sqrt{\frac{f}{8}(Pr^{\frac{2}{3}} - 1)}} \quad (7)$$

Equation 7 use is limited for turbulent flow with Re number ranging between 10^4 and 10^6. However, when the flow is less turbulent with Re less than $10^{4,}$ equation 7 is replaced by:

$$Nu = \frac{\frac{f}{8}(Re - 1000).Pr}{1.07 + 12.7\sqrt{\frac{f}{8}(Pr^{\frac{2}{3}} - 1)}} \quad (8)$$

The flow develops after 15-30 diameters downstream [26], where a thermal boundary layer is formed at the takedown pipe resulting in a higher localized Nu number. The exhaust manifold incorporates bends and restrictions; consequently, the heat transfer region is profoundly affected. The restrictions decrease the boundary layer thickness around the bend and leading to an enhanced heat transfer rate. Hausen H. et al. [27] corrected equation 8 around the bends as

$$\frac{Nu_{bent}}{Nu_{Straight}} = 1 + \frac{21.d_1}{Re^{0.14} d_{bend}} \quad (9)$$

Along with the enhanced heat transfer at the bends, Korremla et al. [24] evaluated the effect of bend on the heat transfer experimentally compared to the development of pulsation on exhaust gases. Results show that heat transfer due to bend effects is

significant compared to pulsating impacts. Chen et al. [23] proposed the use of conventional straight pipe relations and corrected for it by introducing Convective Augmentation Factors (CAF):

$$CAF = \frac{Nu_{effective}}{Nu_{Theoretical}} \tag{10}$$

Manifold runners and takedown pipe exhibit different geometrical features; consequently, the CAF varies for each component of the exhaust manifold system [28]. The exhaust manifold model depends on physical parameters of the manifold; conduction, convection, manifold roughness, and friction along the manifold are estimated and optimized based on experimental results. Manifold parameters affecting the model include:

- Pipe thickness and conduction coefficients
- Exhaust system geometrical design (bends, number of junction and accumulation zones)
- Length of takedown pipe and location of TWC
- Number of connections and flanges

2.3.2.2. Two-Step Lax-Wendorff Numerical Solution of Exhaust Manifold Conservation Equations

The numerical solution for the continuity equations (1), (2), and (4) is based on the two-step Lax Wendorff (LW2) scheme transformation using symbolic vector functions *W*, *V*, and *C*, where the solution at each step provides the density, pressure, and velocity across the exhaust manifold as described in equations 11-13:

$$W(x,t) = \boldsymbol{W} = \begin{bmatrix} \rho \\ \rho u \\ \rho \dfrac{u^2}{2} + \dfrac{p}{k-1} \end{bmatrix} \tag{11}$$

$$F(W) = \begin{bmatrix} \rho u \\ \rho u^2 + p \\ u\left(\rho \dfrac{u^2}{2} + p\dfrac{k}{k-1}\right) \end{bmatrix} \tag{12}$$

$$C(W) = \begin{bmatrix} \rho u \\ \rho u^2 + p \\ u\left(\rho \dfrac{u^2}{2} + p\dfrac{k}{k-1}\right) \end{bmatrix} \frac{d\ lnF}{dx} \begin{bmatrix} 0 \\ g\rho \\ -q\rho \end{bmatrix} \tag{13}$$

The use of symbolic vectors reduces the conservation equations to a first-order hyperbolic PDE, which reduces as:

$$\frac{\partial W}{\partial t} + \frac{\partial F}{\partial x} + C = 0 \tag{14}$$

The LW2 differential scheme uses Taylor expansion of function **W**(x,t) using only the first two terms in direction t; a central difference scheme for $\frac{\partial \boldsymbol{F}}{\partial \boldsymbol{x}}$ and a mean value scheme for vector **W** that returns the pursued vector at mesh point in two steps.

Step 1:

$$W_{i+1/2}^{n+1/2} = \frac{1}{2}(W_{i+1}^n + W_i^n) - \frac{\Delta t}{2\Delta x}(F_{i+1}^n + F_i^n) - \frac{\Delta t}{4}(C_{i+1}^n + C_i^n) \tag{15a}$$

Step 2:

$$W_i^{n+1} = W_i^n - \frac{\Delta t}{\Delta x}\left(F_{i+\frac{1}{2}}^{n+\frac{1}{2}} + F_{i-\frac{1}{2}}^{n+\frac{1}{2}}\right) - \frac{\Delta t}{2}\left(C_{i+\frac{1}{2}}^{n+\frac{1}{2}} + C_{i-\frac{1}{2}}^{n+\frac{1}{2}}\right) \quad (15b)$$

The solution of equations (14), (15a), and (15b) returns a state vector (p, ρ, u) along with the nth spatial mesh at time ith of vectors **W, F,** and **C**. Marching solution in time, computes a new state vector (p, ρ,u) in the discretized spatial variation, which is computed using initial and boundary condition values at the marched time steps.

2.3.2.3. Boundary Conditions for Solving Conservation Equations

The open-end boundary at the exhaust manifold outlet uses the intersection of λ characteristic and the non-dimensional gas velocity defined by U. λ and β right and left of the moving Riemann variables, which are time and space variation variables. If an observer moves with constant velocity, the Riemann variables remain constant to the observer, which results in transforming the PDEs to a set of ODEs in λ and β. Thus, the method of characteristics provides the advantage of simplifying the conservation PDEs to a system of ODEs solved at discrete time steps

The λ characteristic (right moving Riemann variable, i.e., the gas property from propagating in the forward direction step) defines dimensionless distance $X = \frac{x}{L}$ and dimensionless time $Z = \frac{a_0 t}{L}$ as:

$$\frac{dX}{dZ} = U + A \quad (16a)$$

$$\left.\frac{dX}{dZ}\right|_{\lambda} = \frac{\kappa + 1}{2(\kappa - 1)}\lambda - \frac{3 - \kappa}{2(\kappa - 1)}\beta \quad (16b)$$

The β Characteristic (left moving Riemann variable, i.e., the gas property from propagating in the backward direction step) is defined as

$$\frac{dX}{dZ} = U - A \tag{17a}$$

$$\left.\frac{dX}{dZ}\right|_{\beta} = \frac{3-\kappa}{2(\kappa-1)}\lambda - \frac{\kappa+1}{2(\kappa-1)}\beta \tag{17b}$$

where *U* is dimensionless gas speed given by the ratio of gas speed to the isentropic speed of sound $U = {}^{u}/_{a_0}$, and *A* is a dimensionless speed of sound given by the ratio of the speed of sound to an isentropic speed of sound $A = {}^{a}/_{a_0}$.

Flow through exhaust manifold inlet-outlet should satisfy boundary conditions at any particular time step. The inlet-outlet boundary conditions are bonded by physical boundaries, which subsequently prescribe the states of $\lambda \; and \; \beta$ characteristic at the manifold inlet and outlet. March the solution in time, it is necessary to redefine the value of β characteristic at the closed end of the manifold (Cylinder exhaust port end). For the LW2 scheme, β is calculated through interpolation of β characteristic at points 1 and 2 of the mesh, i.e., at, x=0, shown by point 1 in Figure 2-5. The described boundary conditions for $\lambda \; and \; \beta$ are used to determine the states variables (p,ρ,u) at all discretized points across the mesh of the exhaust manifold. Implementing the described boundary conditions requires adding ghost nodes at the boundaries, i.e., N-1 node inside the domain and N+1 outside the domain, to complete the solution along the manifold length.

2.3.3. Exhaust Model Validation

For validation purposes, the model presented in section 2.3.2 is simulated on a shock-tube problem using a constant composition of air. The Shock-tube simulation verifies the model due to the availability of information and shock-tubes' capability to

present discontinuities by the sudden expansion of gasses. Figures 2-6 to 2-9 show a comparison between the LW2 method with the exact solution based on the initial boundary conditions presented in Table 2-2. The exhaust manifold is assumed to be 1 m long with 200 mesh points. Results shown are at t=0.5 ms. The exact solution agrees with the numerical solution using the LW2 method. Results show that LW2 can predict gas properties such as density, pressure, velocity, and temperature.

Table 2-2 Shock-tube initial conditions

ρ_{left}	1.2 kg/m^3	ρ_{right}	0.7 kg/m^3
E_{left}	0.8 MJ/kg	E_{right}	0.2 MJ/kg
V_{left}	0 m/s	V_{right}	0 m/s

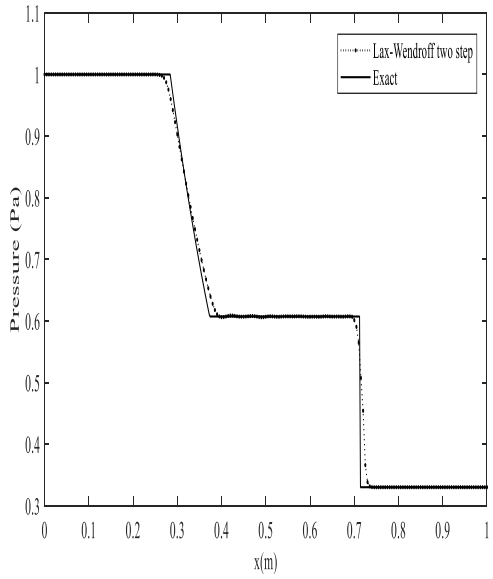

Figure 2-6 Pressure in a shock tube

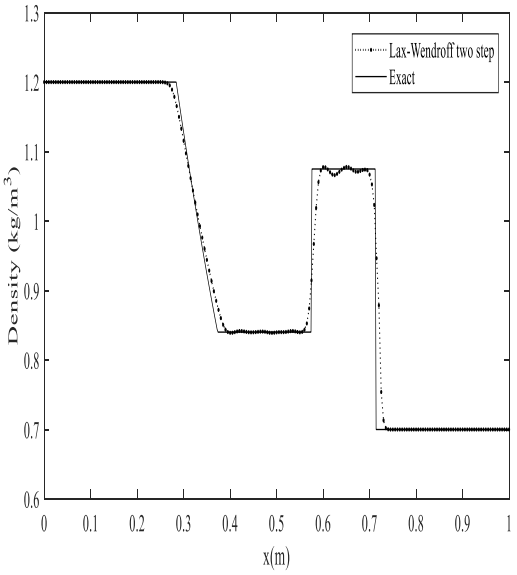

Figure 2-7 Density in a shock tube

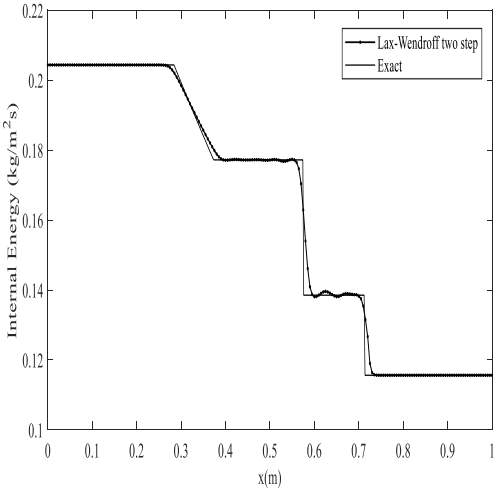

Figure 2-8 Air internal energy in a shock tube

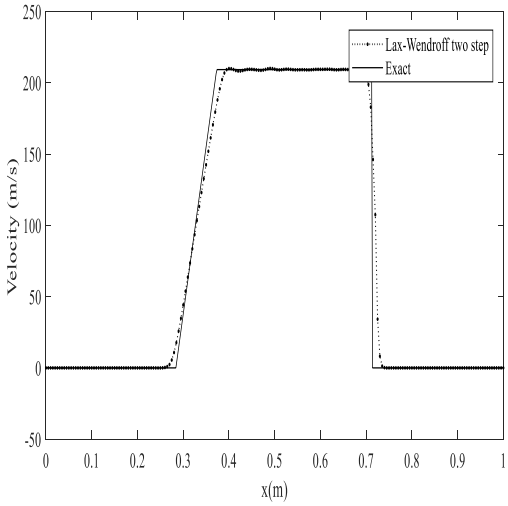

Figure 2-9 Air velocity in a shock tube

2.4. **TWC Model**

A traditional TWC consists of two blocks: (1) reduction catalyst to reduce NO_x to N_2 and (2) oxidation catalyst to oxidize HC (hydrocarbons) and CO to CO_2. The exhaust gases pass through a honeycomb ceramic structure consisting of a thin coating of platinum, palladium, and rhodium known as the wash coat. Figure 2-10 shows a modern monolithic TWC, where the exhaust gas passes through a honeycomb ceramic block, maximizing the surface exposure.

The effectiveness of TWC is due to the oxygen storage materials as CeO_2 ZrO_2, which supports the emission reduction process during rich engine operation. Ceria is a primary component in the TWC for the oxygen storage characteristics, which is essential for both the release of oxygen required for reduction and withholding oxygen for the oxidation reactions. The addition of zirconia also helps promote stability and oxygen storage [30]. The oxygen stored in TWC helps oxidize the CO to CO_2 and combust unburnt hydrocarbons to CO_2 and water.

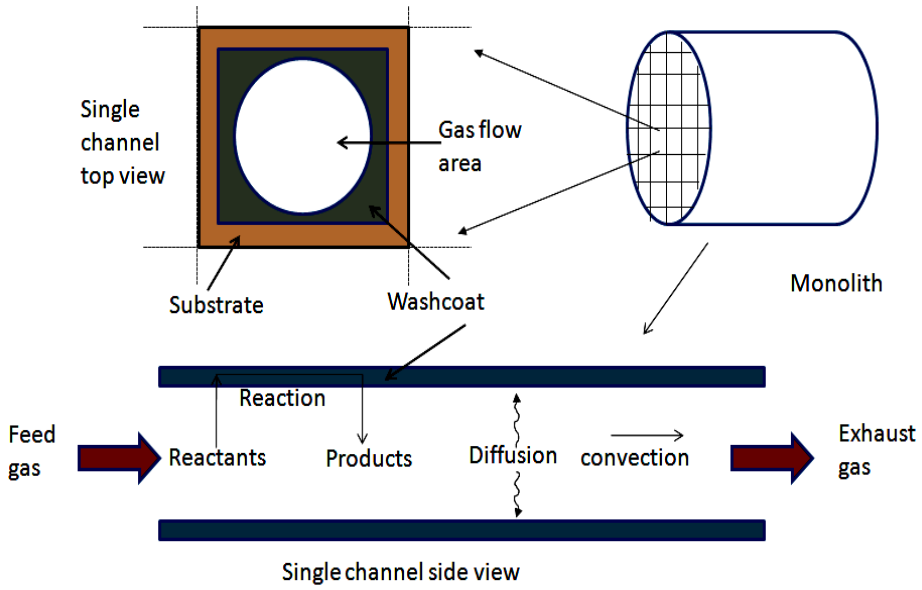

Figure 2-10 Typical underbody TWC monolith structure

2.4.1. Background on TWC Modeling

In a monolith reactor as the TWC, various physicochemical processes occur, where the exhaust gas flows through the channels of the monolith. At the TWC, exhaust gases are transported along the axial direction of gas flow, where the reactants species diffuses through the wash coat catalyst. The reaction at the TWC can be assumed as exothermic; consequently, heat transfers to the surroundings through both convection and conduction. Reversely, the products out of the TWC transports to the bulk exhaust gases employing mass transfer mechanisms. The complexity of the predictive models depends on the accuracy and complexity needed; these models range from simple 1D models to intricate 3D models. Accurate prediction for the conversion efficiency of a TWC depends on the inlet conditions specified.

The chemical process dynamics within TWC, primarily during the transient stages of engine operation, indicate that chemical kinetics are still obscure regarding oxygen storage when coupled with the AFR ratio. Normalized AFR, λ, is defined in two regions of rich operation when $\lambda<1$, and lean operation when $\lambda>1$, as shown by Figure 2-11. TWC efficiency is optimal at stoichiometry [22]. Engine acceleration and braking cause deviations from this optimum value.

Developing an efficient TWC model lies in understanding the strategic principles of TWC kinematics of reactions. Detailed analysis and parametric study of the oxidation/reduction process expose the underlying principles for optimizing TWC performance based on AFR. A slight variation of the AFR reworks the simulated converter work making it inefficient in some cases; subsequently, for optimized emission reduction, the AFR should fall in a narrow stoichiometric [29].

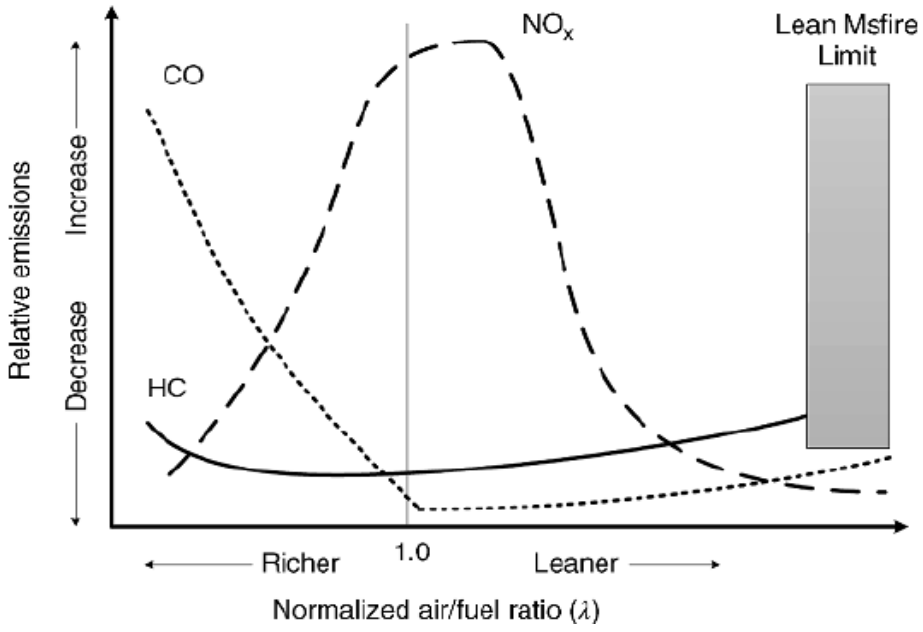

Figure 2-11 Emission formation as a function of normalized AFR

Attempts to capture the dynamic model in modern studies of system efficiency are slowed down by the rich bias of feed gas oxygen sensors [20], which imposes the need for the integration of various vehicle components. Studies showed that when AFR (λ) = 0.953, CO conversion is unpredictable due to high O_2 conversion, affecting the subsequent catalytic reaction. Alternatively, NO_x reduction is high on the rich side [30]. The dynamic response of the upstream and downstream Universal Exhaust Gas Oxygen (UEGO) is critical for developing such models. Grizzle et al. [31] presented a dynamic model that accounts for the upstream rich bias that forces the system towards the lean side. As a result, the establishment of exhaust gas exchange dynamics is essential for modeling the process and predicting vehicle emission behavior.

TWC models are divided into three major categories [32]; complex models that model the chemical reactions, thermo-fluid relations, and the catalytic reactions in a TWC; these models present high complexity. The second category is a global reactions approach, giving elementary kinetics and wash-coat materials. The last category is a control-oriented approach [33]. Control-oriented models that only focus on oxygen storage omit structural characterizations of TWC; thus, oxygen storage models result in inaccurate estimations primarily when different scopes of operation are implemented [34]. On the other hand, 1D models achieve spatial and time variations through a reduced set of PDEs, or ODEs, while preserving the integrity of the TWC structure.

For instance, Voltz et al. [35] used a global kinetic reaction mechanism involving CO oxidation using a platinum base catalyst. The global reaction kinetic model developed by Voltz is used extensively by other researchers for modeling CO conversion in platinum TWC. Hayes et al. [36] used a global reaction kinetic model of four global reaction mechanisms and a phase model of two phases to model the TWC performance. The study investigated the model's sensitivity to gas inlet temperature during transient phases of operation. The study has neglected the wash coat diffusion effects and assumed a pseudo-steady state for the solid phase concentration of the catalyst.

Similarly, Siemund et al. [37] verified a four reaction global kinetic model experimentally. The model additionally included both CO and NO reduction. The mass and energy conservation used a quasi-steady-state assumption and a transient form for robust energy conservation. Dubien et al. [38] extended the global kinetic model to nine reactions, including hydrogen chemistry, water-gas shift reaction, and steam reforming

reactions. Dividing the fuel into two categories, slow- and fast-burning fuel species allows the expansion.

Comprehensive model data shows that catalytic converters efficiency is temperature dependent, which questions the validity of existing models within different operating temperatures other than proposed in the studied cases. Thermo-chemical analysis of the effect of temperature and variance of enclosed species in TWC is improved by the migrating of (ce,Zr)x-O_2 rich gain after aging treatment [39]. The use of CZHal showed improvement in catalyst efficiency with decreased light-off temperature to the C_3H_8, NO_x, and CO emissions [40]. The cubic zirconia praseodymium modified as CZP8 plates showed higher thermal stability and greater oxygen storage capacity, and improved reduction efficiency of emission gasses than using Pd/CZP_8.

A common practice in simulating TWC performance is to consider it as an independent component. Typically, a steady synthetic gas blend of fixed composition with constant temperature is passed at the inlet, while real conditions consist of unsteady gases of fluctuating temperatures, pressures, and compositions. It deems necessary to include the combined interactions between the various components: engine, exhaust manifold, and TWC. Models and relationships between different interacting compounds within TWC focus on optimizing chemical models and defining the descriptive behavior of species. The comprehensive development and expansion of the current models present the form of chemical and mathematical formulation for TWC physicochemical phenomenon helps capture the catalyst phenomenon in conjunction with the internal combustion model. The underlying thermodynamics of TWC investigates the

temperature dependence of existing TWC through lab experiments and mathematical modeling. Most of the thermal models presented are incapable of precisely modeling the efficiency at cold start, which offers a vibrant area of investigation. Results from this area are of great importance to AFR active control system [33].

2.4.2. 1-D TWC Mathematical Model Development

The present work improves the current 1D model Pankaj [43] proposed, which models a TWC on a control-oriented basis but preserves the optimum representation of chemical reaction kinetics occurring within an automotive TWC. Additionally, the current model incorporates fractional oxygen storage (FOS) and total oxygen storage capacity (TOSC).

The TWC can simplify from a three-dimensional to one-dimensional model for control-based models; by assuming symmetry. Ignoring variations along the radial direction and only accounting for axial changes further reduces the model to a 1D model [41]. The TWC model studies a single channel of the honeycomb structure, which is assumed to represent the whole catalyst block fully. Also, the model assumes that the reaction only takes place at the wash coat by applying mass and energy balance to the single channel of the TWC.

The model below will study a single channel of the honeycomb structure which is assumed to be a full representation of the whole catalyst block. Also, the reaction is assumed only to take place at the wash coat. Applying mass and energy balance to the system which is a single channel of the TWC.

The species balance is given by:

$$\frac{d\boldsymbol{X}_{fm}}{dt} = -\frac{\langle u \rangle}{L}\left(\boldsymbol{X}_{fm} - \boldsymbol{X}_{fm}^{in}(t)\right) - \frac{\boldsymbol{K}_{mo}}{R_{\Omega}}\left(\boldsymbol{X}_{fm} - \langle \boldsymbol{X}_{wc} \rangle\right) \tag{18}$$

The gas species balance in the wash coat:

$$\epsilon_w \frac{d\langle \boldsymbol{X}_{wc} \rangle}{dt} = \frac{1}{C_{Total}} \boldsymbol{\nu}^T \boldsymbol{r} + \frac{\boldsymbol{k_{mo}}}{\delta_c}\left(\boldsymbol{X}_{fm} - \langle \boldsymbol{X}_{wc} \rangle\right) \tag{19}$$

The overall mass transfer is given by the addition of the external and internal mass transfer coefficient:

$$K_{mo}^{-1} = K_{mi}^{-1} + K_{me}^{-1} \tag{20}$$

The mass transfer of the external mass is given by:

$$\boldsymbol{k}_{me} = \frac{D_f Sh}{4R_{\Omega}} \tag{21}$$

$$Sh_i = Sh_{i,\infty} + (I + \Lambda\Phi)^{-1}\Lambda\Phi^2 \tag{22}$$

$$\Phi_{ii}^2 = \frac{\delta_c^2}{D_{s,i}} k_{i,eff} \tag{23}$$

The energy balance is given for the fluid as:

$$\rho_f Cp_f \frac{dT_f}{dt} = -\frac{\langle u \rangle \rho_f Cp_f}{L}\left(T_f - T_f^{in}(t)\right) - \frac{h}{R_{\Omega}}\left(T_f - T_s\right) \tag{24}$$

The wash coat energy balance is given by:

$$\delta_w \rho_w Cp_w \frac{dT_s}{dt} = h\left(T_f - T_s\right) + \delta_c \sum_{i}^{Nr} r_i(-\Delta H_i) \tag{25}$$

Oxygen storage in ceria is given by:

$$\frac{d\theta}{dt} = \frac{1}{2TOSC}(r_{store} - r_{release}) \tag{26}$$

Initial conditions are shown in Table 2-3:

Table 2-3 Initial conditions

component	Condition	Time
$\boldsymbol{X}_{fm,j}$	$X_{fm,j}^{0}$	0
$\langle \boldsymbol{X}_{wc,j} \rangle$	$X_{fm,j}^{0}$	0
T_f	T_f^0	0
T_s	T_s^0	0

During the rich side of the cycle operation, CO cannot be fully oxidized due to deficiency of oxygen. However, CO can be oxidized through water-gas shift reaction utilizing water over the Ceria base and precious metal loading. This reaction also produces H_2 which can be useful for the reduction of NO.

$$CO + H_2O \leftrightharpoons CO_2 + H_2$$

In order for the reaction to take place, the four reactants and products should be present thus promoting the presence of H_2 in the exhaust and reducing the presence of H_2O. In the development of this model, the water gas shift reaction needs to be further developed to accurately predict TWC behavior. The water gas shift reaction, in essence, poses a problem for the design of a robust controller since it affects the HEGO sensors capable of accurately predicting the oxygen content of the exhaust gases by impacting the voltage generated in the HEGO sensor itself.

2.4.3. TWC Kinetic Reduced Model Development

Kinetic models for TWC vary in different ranges of equations depending on the accuracy. For on-board diagnostics (OBD), the models are simpler yet represent the catalyst kinetics. The simple model accounts for the fractional oxygen storage (FOS) and total oxygen storage capacity (TOSC) instead of taking each emissive gas constituent into account. The catalyst in this work consists of Rhodium (Rh), Platinum (Pt), and Palladium (Pd). Table 2.4 shows the numerical constants for TWC simulation. Table 2-5 shows the global reaction in the TWC. The complexity of the model reduces when abridging individual species (CO, CO_2, NOx, and HC) to collective grouping in terms of reductants and oxidants.

$$[A] = \left(2 + \frac{y}{2}\right)\left[CH_y\right] + [CO] + [H_2] + \frac{3}{2}[NH_3] \tag{27}$$

$$[O_x] = [O_2] + \frac{1}{2}[NO] \tag{28}$$

$$[AO] = [CO_2] + [H_2O] \tag{29}$$

Equations 27 to 29 represent the stoichiometric relations for the reactions that yield the production of $\mathrm{CO_2}, \mathrm{H_2O}, \mathrm{N_2}$. Table 2-6 presents the specific reaction rates and enthalpies, where $\left[CH_y\right]$ y= 1.875 which is a general representation of hydrocarbon present in the gasoline [43].

Table 2-4 Numerical constant used for TWC simulation

Constant	Value
R_Ω	181x10^{-6} m
δ_c	3x10^{-5} m
δ_s	6.35 x10^{-5} m
k_f	0.0386 W/m.K
Cp_f	1068 J/Kg. K
Cp_w	1000 J/Kg. K
ρ_w	2000 kg/m^3
ϵ_w	0.41
τ	8.0
Sh	3.21
Nu	3.21
Sh, i	2.64
Λ	0.57

Table 2-5 Global reaction in TWC

	Reaction	-$\Delta H\ (700K)\ (\frac{kJ}{mol})$ x10^3
1	$CO + \frac{1}{2}O_2 \longrightarrow CO_2$	-283
2	$H_2 + \frac{1}{2}O_2 \longrightarrow H_2O$	-242
3	$C_3H_6 + \frac{9}{2}O_2 \longrightarrow 3CO_2 + 3H_2O$	-1920
4	$NO + CO \longrightarrow CO_2 + \frac{1}{2}N_2$	-373
5	$NO + H_2 \longrightarrow H_2O + N_2$	-3.32
6	$CO + H_2O \leftrightarrows CO_2 + H_2$	-41
7	$C_3H_6 + 3H_2O \leftrightarrows 3CO + 6H_2$	374
8	$CO + Ce_2O_4 \longrightarrow Ce_2O_3 + CO_2$	-183

9	$\frac{1}{9}C_3H_6 + Ce_2O_4 \longrightarrow Ce_2O_3 + \frac{1}{3}CO_2 + \frac{1}{3}H_2O$	-114
10	$Ce_2O_3 + \frac{1}{2}O_2 \longrightarrow Ce_2O_4$	-100
11	$Ce_2O_3 + NO \longrightarrow Ce_2O_4 + \frac{1}{2}N_2$	-190

Table 2-6 Reduced lumped order reaction rates for O_2 storage and release

#	Reaction	Rate ($\frac{mol}{m^3 s}$)	$-\Delta H$ ($\frac{kJ}{mol}$)
1	A+$\frac{1}{2}O_2 \longrightarrow AO$	$r_1 = a_c \frac{A_1 \exp\left(\frac{-E_1}{RT_s}\right) X_{o_2} X_A}{T_s(1 + K_{a1}X_A)^2}$	283
2	$Ce_2O_3 + \frac{1}{2}O_2 \longrightarrow Ce_2O_4$	$r_2 = a_c A_2 \exp\left(\frac{-E_2}{RT_s}\right) X_{o_2}(1-\theta)$	100
3	A+$Ce_2O_4 \longrightarrow Ce_2O_3 + AO$	$r_3 = a_c A_3 \exp\left(\frac{-E_3}{RT_s}\right) X_{o_2}\theta$	183

2.4.4. TWC Model Validation

The developed TWC model calculates the reduced tailpipe emissions based on experimental inlet data. The current work modifies the model developed by Pankaj [41] to replace empirical data as input with the out-of-cylinder emissions obtained through the SI engine model, which allows a fully integrated emission modeling. Table 2-7 shows the TWC used parameters.

The model output is compared with measured emission data, as shown in Figures 2-12 and 2-13. The model calculated emissions after the TWC (red) is compared

with experimentally measured data (black). The emissions divided into two groups, O_2 concentration and reductants (NO, CO, UHC). The model prediction is consistent with experimental measurements during operation segments. When the changes are rapid, the maximum error is around 6% for O_2 prediction presented by the oxidant breakthrough delayed for transition from rich to lean and 12% for reductants. When the changes are slower the error reduces to around 4%. The conversion is low for lean feed around 25% and goes to 99% for rich phases of the cycle. The conversion is limited by the limiting reagents concentration, the delay between the inlet and outlet represents the transition of ceria between Ce^{3+} and Ce^{4+} and vice versa.

Table 2-7 TWC parameters

Parameter	Value
TWC dimension	4x4x3.1
Wash coat loading ratios (Pd:Pt:Rh)	0.69:0:1
Loading (g/ft^3)	68
Cell per square inch/ thickness-wall	9000/25

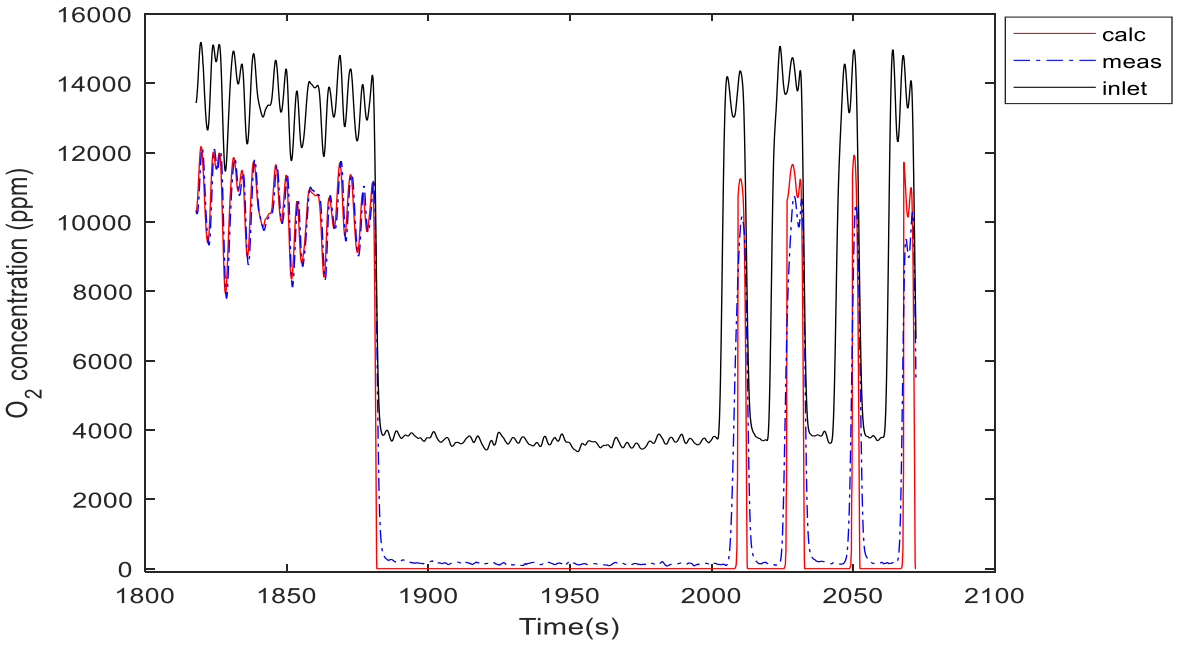

Figure 2-12 Comparing TWC model with experimental results Oxygen

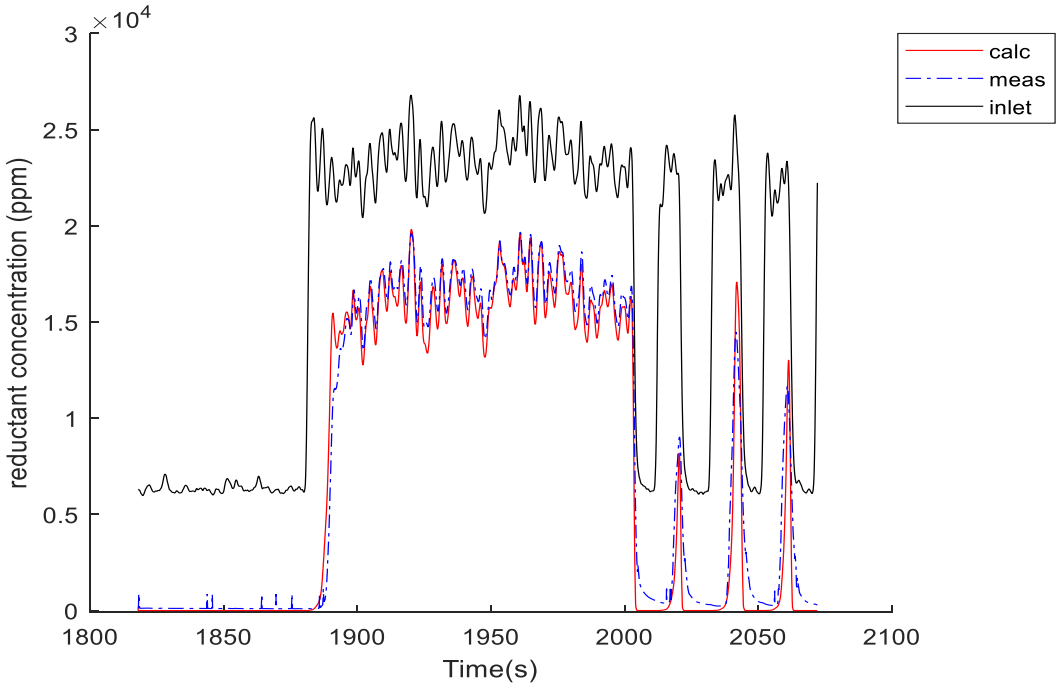

Figure 2-13 Comparing TWC model with experimental results reductants

2.5. SI Engine Model

Four-stroke SI engines consist of four concurrent steps: intake, compression, Power (expansion during combustion), and exhaust stroke. In the intake stroke, the first stroke introduces the air-fuel mixture into the engine cylinder. The piston then moves from the Bottom Dead Center (BDC) to the Top Dead Centre (TDC), compressing the compression stroke's combustion mixture. The BDC and TDC are the piston positions concerning the crankshaft expressed in terms of crank angle. At the end of the compression stroke, the spark initiated via the spark plug ignites the mixture; this, in turn, causes a controlled explosion which initiates the piston to move to BDC (power stroke). The power stroke produces the power required for the crankshaft to rotate and transfer it to the transitional components such as flywheel, transmission, and differential. The piston then moves to the top dead center (TDC) position again. The exhaust valves are open via the camshaft to evacuate the exhaust gases left in the cylinder, which are the by-product of the combustion process (exhaust stroke).

2.5.1. Background on SI Engine Models

The momentum towards engines designed to have optimal fuel efficiencies and minimum emissions has always been an aim for developing new engine technologies. A physical model capable of appropriating the phenomenon of combustion within the engine cylinder and the formation of by-products is quintessential to meet the ever-increasing legislation on vehicle emissions and engine optimization. There are three major approaches in modeling in-cylinder combustion; (1) non-predictive combustion model, which uses a burn rate as a function of crank angle. In this methodology, the

prescribed burn rate is followed regardless of the conditions in the cylinder, assuming that there is a sufficient quantity of fuel input into the cylinder to support the burn rate. In this case, the model ignores the residual fraction of fuel and the injection timing. This approach is suitable as long as the model is used to study a phenomenon that has little effect on the burn rate. For instance, the influence of intake manifold runner lengths on volumetric efficiency does not require any prediction of the burn rate.

Non-predictive model is not ideal when the model's intended use is to study a variable that has a direct and significant effect on the burn rate. Heywood et al. [42] and Griffin et al. [43] utilized three-dimensional flow characteristics to model combustion via heat addition in a constant volume. Dinler et al. [44] and Seifert [45] used the energy balance method to quantify the flow fields for a four-stroke SI engine. A mean value model (MVM) developed by Hendricks et al. [46] can predict the various internal engine variables over their mean values, which helped reduce complexity and computation time. Pratheeba et al. [47] and Kumar et al. [48] used a mathematical approach to develop a low dimensional model of the combustion process in an SI engine.

Predictive models consider the inter-dependent variable to establish homogeneity in terms of inputs and outputs. The added complexity is the main reason for their slow performance. Predictive models also require more data, such as measured pressure profiles, ambient conditions, and temperature profiles. These models generally require calibration to predict burn rate from appropriate inputs such as pressure, temperature, equivalence ratio, and the residual fraction from measurement data to provide an accurate result.

A semi-predictive combustion model may be a good substitute for a predictive model. In cases the model is sensitive to the significant variables that influence combustion rate, these models respond appropriately to changes in variables. A predictive or semi-predictive combustion model is more appropriate for integrated modeling so that the burn rate will react appropriately to a difference in the variables of interest [59] [60].

The low-order modeling of the in-cylinder combustion phenomenon utilizes the spatially averaged convection-diffusion-reaction model for predicting the combustion dynamics of an SI engine along with pollutant formation. The prediction of fuel consumption alongside emission lies in the modeling of multivariable engine components. The current work implements the first principles-based low dimensional in-cylinder combustion model, including after-treatment models.

2.5.2. SI Engine Mathematical Model Development

Current work builds on spatially averaged three-dimensional convection-diffusion-reaction (CDR) model developed by Bhattacharya et al. [49]. Below are assumptions to reduce the overall model complexity and computation time:

- Gasoline is a complex mixture of hydrocarbons that has to be simplified. Hence, 80% fast burning (Iso-Octane) and 20% slow burning $(CH_2)_2$, which reflects the similar properties to gasoline when C:H ratio in the order of 1:1.875. This simplifications aid in predicting the total hydrocarbons being utilized after combustion and the subsequent unburnt hydrocarbons.

- Due to the complexity involved in modeling and predicting the different species included in the combustion process, the model utilizes global reaction kinetics, which can capture the significant directions of the chemical reactions. (Westbrook et al [50]., Marinov et al [51].)
- The combustion chamber is assumed to be a tubular reactor with a single chamber with uniform temperature and concentration profiles throughout.
- The combustion chamber is comprised of two control volumes, one before combustion and one right after the exhaust stroke.
- The mixing times within the combustion chamber are not considered to be fast, and hence two mixing times are introduced to account for the mixing between the reactants before the combustion process and the by-products formed.
- The combustion chamber is divided into N number of cells that are interfacing.
- Each cell employs a convection-diffusion-reaction (CDR). The Lyapunov-Schmidt technique considers the overall concentration and the averaged volume concentration of the species entering the combustion chamber.

The instantaneous cylindrical volume V (t) at any moment during the engine cycle can be co-related to the crank angle via equation:

$$\frac{V(t)}{V_c} = 1 + 0.5(r_c - 1)[\hat{R} + (1 - (cos\,\theta\,(t))) - (\hat{R}^2 - (sin^2\,\theta\,(t)))^{\frac{1}{2}}] \quad (21)$$

V_c= the clearance volume r_c= compression ratio $\hat{R}$= ratio of connecting rod length to crank radius $\theta(t)$ = crank angle at time. On differentiating equation 21 with respect to time again, we can obtain the change of volume of the piston-cylinder assembly as:

$$\frac{dV}{dt} = V_c(0.5(r_c - 1)[sin\,\theta + \frac{sin\,\theta\, cos\,\theta}{\hat{(R^2 - sin^2\,\theta)^{\frac{1}{2}}}}])\Omega \quad (22)$$

$\Omega = \frac{d\theta}{dt}$ = angular speed. It is important to note that for the development of low dimensional model the angular speed was kept constant. This was done to ascertain baseline readings of one specific engine RPM speed which in conjunction was directly related to the reaction kinetics specific to certain parameters of the engine such as the air-fuel ratio. The air flow rate was computed based on previous work by Franchek et al. [52] involving first principles based on the air path dynamic model; this is shown from:

$$Q_{in}^{air} = \eta_{vol}\frac{V_d\Omega}{4\pi} \quad (23)$$

$$V_d = (r_c - 1)V_c \quad (24)$$

$$\eta_{vol} = E\frac{k-1}{\gamma} + \frac{r_c - (\frac{P_{amb}}{P_{man}})}{\gamma(r_c - 1)} \quad (25)$$

Ideal gas laws at standard temperature and pressure are used in computing the air flow conditions. With a specific throttle position opening the amount of air entering can be co-related to a specific flow rate; however, the fuel flow rate can then be computed using:

$$Q_{in}^{fuel} = \frac{1}{\lambda(10.6 - 7.6x_e)}Q_{in}^{air} \quad (26)$$

The concentration of gases entering the combustion chamber can then be computed using standard temperature and pressure conditions at the manifold with the specific λ value. The volumetric flow rate than for the exit via the exhaust valve can then be computed using:

$$Q = C_d A_{th}\sqrt{2\frac{(P - Pout)}{\rho}} \quad (27)$$

It is important to note that backflow into the cylinder cavity after exhaust stroke is negated and the flow is presumed to be flowing outwards or 0 in the case when the exhaust valves are closed.

2.5.3. Species Balance for in-cylinder combustion

Taking the cylinder as a system of concern; species balance helps to compensate for the changes in concentration due to mass crossing the various system boundaries. The system defined incorporates two regions; the major combustion chamber of the cylinder accompanied by a crevice area where leaks of HC would occur between the cylinder and piston. This is represented by :

$$\frac{d(\langle C_j \rangle)}{dt} = \frac{1}{V}\left[F_j^{in} - F_j + \sum_{i=1}^{N_R} v_{i,j} R_i(\langle C \rangle)V - \langle C_j \rangle \frac{dV}{dt} - F_{j,cr}\right] \frac{d(C_{cr,j})}{dt} = \frac{1}{V_{cr}}\left[F_{j,cr} + \sum_{i=1}^{N_R} v_{i,j} R_i(C_{cr})V_{cr}\right] \quad (28)$$

The cylinder model can be modeled as an ideal perfectly mixed CSTR as explained by Bhattacharya et al., [9] when the limit of mixing times diminishes the above model can be applicable. In order to compensate for non-uniformity in the cylinder, the interaction between the mean concentrations is represented by the dimensionless mixing times $t_{mix,1}$ and $t_{mix,2}$. When the mass input is perfectly mixed before being introduced to the cylinder and no interference between inlet and exhaust valves the mixing time $t_{mix,2}$ approaches zero thus validating the CSTR assumption. The diffusivity of the reactant species, engine rotation, and the velocity profile in the cylinder is presented by $t_{mix,1}$ the later assumption is represented by:

$$C_{m,j} - \langle C_j \rangle = t_{mix,2} C_{m,j}^{in} \quad (29)$$

In conjunction with previous equations, the exchange and concentration flow rate between the two volumes; the crevice and combustion volume of a cylinder. The volume of the crevice is assumed to be 3.5% of the clearance volume, the flow of mixture into or out of the crevice is a function of the cylinder pressure and inversely proportion. Following the ideal gas presumption; ideal gas equation will be used to find the pressure within the crevice.

$$F_{j,cr} = Q_{cr}(aC_{m,j} - (1-a)C_{cr_j}) \tag{30}$$

The value of a solely depends on the flow direction, 1 for flow into crevice and 0 otherwise.

Gasoline being a complex mixture has close to 500 or more complex hydrocarbons. A lumped species modeled capable of capturing the characteristic combustion sequence of all major hydrocarbon groups (n-alkanes, branched, aliphatic and aromatic) is fundamental, however, in this work hydrocarbons are subdivided into fast burning (Iso-Octane n-alkane group) 80% and slow burning $(CH_2)_2$ 20% which reflects the similar properties to gasoline when C:H ratio in the order of 1:1.875. The global kinetics for iso-octane n-alkane group and ethanol mixture are taken into consideration. This help defines the orders of reaction along with the specific kinetic constants. This can be seen in table 2-8. In the table the reactions each represent the combustion breakdown of fuel (1, 2 and 7), the reduction reaction of CO to CO2 (3b and 3f), the water-gas shift reaction (4f and 4b), NOx formation (5) and lastly the combustion of the fuel profile ethanol if fuel blend is used. Table 2-9 give the global kinetics for combustion.

Table 2-8 Woschni's correlation parameters

Engine cycle period	C_1	C_2
Gas exchange period	6.18	0
Compression period	2.28	0
Combustion and expansions	2.28	3.24×10^{-3}

Table 2-9 Global kinetics for combustion

#	Reaction	Order of reaction	A $\times 10^{11}$	β	E_a
			(molcm,s^3)		
1 [50]	$C_8H_{18} + \frac{17}{2}O_2 \longrightarrow 3CO + 4H_2O$	$[C_8H_{18}]^{0.25}[O_2]^{1.5}$	5.7	0	30000
2 [52]	$(CH_2)_n + nO_2 \longrightarrow nCO + nH_2$ n=1.875	$[(CH_2)_n]^{0.1}[O_2]^{1.85}$	1.2	0	30000
3f [50]	$CO + \frac{1}{2}O_2 \longrightarrow CO_2$	$[CO][H_2O]^{0.5}[O_2]^{0.25}$	3980	0	40000
3b [50]	$CO_2 \longrightarrow CO + H_2O$	$[CO_2]$	0.008	0	40000
4f [53]	$CO + H_2O \longrightarrow CO_2 + H_2$	$[CO][H_2O]$	27.5	0	20000
4b [53]	$CO_2 + H_2 \longrightarrow CO + H_2O$	$[CO_2][H_2]$			
5f [42]	$N_2 + O_2 \longrightarrow 2NO$	$[O_2]^{0.5}[N_2]$	600000	-0.5	137281
5b [42]	$2NO \longrightarrow N_2 + O_2$	$[NO]^2[O_2]^{-0.5}$			
6 [51]	$H_2 + \frac{1}{2}O_2 \longrightarrow H_2O$	$[H_2][O_2]^{0.5}$	180	0	34500
7 [50]	$C_2H_5OH + 2O_2 \longrightarrow 2CO + 3H_2O$	$[C_2H_5OH]^{0.15}[O_2]^{1.6}$	18	0	30000

2.5.4. Derivation of energy balance for in-cylinder combustion

Following species balance, energy balance is performed through utilizing the first law of thermodynamics, applied to the cylinder model. Energy balance will be performed based on an open system analysis given by the equations below.

$$\dot{Q}_{heat} - \dot{W}_s + \sum_{j=1}^{N_c} F_j^{in} H_j^{in} - \sum_{j=1}^{N_c} F_j H_j = \frac{\partial \hat{E}}{\partial t} \tag{31}$$

Ignoring changes in K.E and P.E in the total energy equation and differentiating with respect to time will yield:

$$\frac{d\hat{E}}{dt} = \sum_{j=1}^{N_c} N_j \left(\frac{dH_j}{dt}\right) + \sum_{j=1}^{N_c} H_j \left(\frac{dN_j}{dt}\right) - \frac{d}{dt}\left(\sum_{j=1}^{N_c} N_j RT\right) \tag{32}$$

Applying mass balance to the given system results in:

$$\frac{dN_j}{dt} = F_j^{in} - F_j + \sum_{i=1}^{N_R} v_{ij} R_i(\langle C \rangle) V_R \tag{33}$$

Substituting mass balance into total energy balance equation:

$$\frac{d\hat{E}}{dt} = \sum_{j=1}^{N_c} N_j Cp_j \left(\frac{dT}{dt}\right) - \sum_{j=1}^{N_c} N_j R \left(\frac{dT}{dt}\right) - RT \sum_{j=1}^{N_c} \frac{dN_j}{dt} + \sum_{j=1}^{N_c} H_j \left(F_j^{in} - F_j + \sum_{i=1}^{N_R} v_{ij} R_i(\langle C \rangle) V_R\right) \tag{34}$$

Substituting the above results into the overall energy balance and simplifying:

$$\dot{Q}_{heat} - \dot{W}_s + \sum_{j=1}^{N_c} F_j^{in}\left(H_j^{in} - H_j\right) - \sum_{i=1}^{N_R} R_i(\langle C \rangle) V_R * \left(\Delta H_{R,i}\right)_T + RT \sum_{j=1}^{N_c} \frac{dN_j}{dt} = \sum_{j=1}^{N_c} N_j Cp_j \left(\frac{dT}{dt}\right) - \sum_{j=1}^{N_c} N_j R \left(\frac{dT}{dt}\right) \tag{35}$$

This can be reduced further by assuming the shaft work is the same as the work done by the piston. Work was done by piston: $\left(P\dot{V}_R\right)$

$$\frac{dT}{dt} = \frac{1}{V_R \sum_{j=1}^{N_c} \langle C_j \rangle \langle C_{pj-R} \rangle} \left[\dot{Q}_{sprak} - \dot{Q}_{coolant} - P\dot{V}_R + \sum_{j=1}^{N_c} F_j^{in} \left(H_j^{in} - H_j \right) + \right.$$

$$\left. \left(\sum_{i=1}^{N_R} R_i(\langle C \rangle) V_R \left(-\Delta H_{R,i} \right)_T \right) + RT \sum_{j=1}^{N_c} \frac{dN_j}{dt} \right] \quad (36)$$

2.5.5. Energy balance for in-cylinder combustion

For energy balance within the combustion chamber, it is important to assume that ideal gas behavior is exhibited. The overall energy balance of the combustion process can be utilized via the established in-cylinder species balance and temperature variation profile model for parameters inside the periphery of the combustion chamber. The overall energy balance equation can be presented by:

$$\frac{dT}{dt} = \frac{1}{V_R \sum_{j=1}^{N_c} \langle C_j \rangle \langle C_{pj-R} \rangle} \left[\dot{Q}_{sprak} - \dot{Q}_{coolant} - P\dot{V}_R + \sum_{j=1}^{N_c} F_j^{in} \left(H_j^{in} - H_j \right) + \right.$$

$$\left. \left(\sum_{i=1}^{N_R} R_i(\langle C \rangle) V_R \left(-\Delta H_{R,i} \right)_T \right) + RT \sum_{j=1}^{N_c} \frac{dN_j}{dt} \right] \quad (37)$$

In the previous formula $\dot{Q}_{sprak}$ represents the externally supplied energy by the spark which have the function of lighting up the cylinder mixture. $\dot{Q}_{coolant}$ represents the heat transferred out of the cylinder block. At temperature T the heat of reaction is imbedded into the equation as$\left(-\Delta H_{R,i}\right)_T$. While using the above equation caution should be taken in applying the balance based on the boundary condition which is the stage of engine cycle.

2.5.6. Heat transfer

To tackle the heat transfer phenomenon within the chamber of the cylinder a simplistic approach can be taken in which the different modes of heat transfer can be considered. Radiation and convection are the modes of heat transfer from the

combustion process to the internals of the combustion chamber wall itself via the combustion gases. Conduction phenomenon is then utilized for the heat transfer between the cylinder walls and the outer lining of the combustion chamber.

Heat transfer from the gas to the cylinder:

$$\dot{q}_g = h_{c,g}\left(T - T_{w,g}\right) + \sigma\varepsilon\left(T^4 - T_{w,g}^4\right) \tag{38}$$

Heat transfer by conduction:

$$\dot{q}_w = \frac{k(T_{w,g} - T_{w,c})}{l} \tag{39}$$

Heat transfer by convection from wall to coolant:

$$\dot{q}_c = h_{c,c}\left(T_{w,c} - T_c\right) \tag{40}$$

Heat flux:

$$\dot{q} = \frac{(T - T_c)}{\left(\frac{1}{h_{c,g}} + \frac{1}{k} + \frac{1}{h_{c,g}}\right)} \tag{41}$$

Woschni's correlation to define the heat transfer from gas Heywood et al.[42].

$$h_{c,g} = 3.26B^{-0.2}p^{0.8}T^{-0.55}w^{0.8} \tag{42}$$

W represents the average gas velocity in the cylinder:

$$w = C_1 S_p + C_2 \frac{V_d T_r}{p_r V_r}(p - p_m) \tag{43}$$

2.5.7. SI-Model Validation

The utilized SI combustion engine low-dimension model is reliable with high computational efficiency. The multi-cylinder model is an improved version of the work presented by Pankaj [52]. The main features of the model are:

- A four-mode low dimensional model
- Lumped parameter ordinary differential equation

- Two mixing times for reaction-diffusion
- Regulated emission representation: HC, CO, NOx
- In-cylinder temperature and pressure

The combination work includes expansion work to the base SI-Engine model to include the effect of multi-cylinders, mainly through considering each cylinder's firing order and the gas exchange sequence. The model adopts a V6 engine configuration and 60° crank angle difference for comparison purposes and experimental validation constraints. Table 2-10 shows the firing order and the phase difference of the four strokes of the engine. Based on a single-cylinder engine configuration, the base combustion model predicts the in-cylinder and out-of-cylinder emissions. The present work expands on the single-cylinder to include three-cylinder emissions, which represents a single bank of the engine. For analysis and comparison purposes, the study considers only one bank for analysis. Appendix A provides a detailed presentation of the base model. The main features of the model are:

- Approximated transverse gradients
- Multiple concentration modes for internal and external mass transfer
- A spatial average for axial length
- Lumped oxidants and reductants

The out-of-cylinder emission based on the SI engine model with engine parameters given in Table 2-11.

Table 2-10 Firing sequence for a 60-degree phase difference

	Bank 1			Bank 2		
	Cylinder 1	**cylinder 2**	**Cylinder 3**	**Cylinder 4**	**Cylinder 5**	**Cylinder 6**
0	Suction				Exhaust	
60			Exhaust	Suction		
120		Suction				Exhaust
180	Compression				Suction	
240			Suction	Compression		
300		Compression				Suction
360	Power				Compression	
420			Compression	Power		
480		Power				Compression
540	Exhaust				Power	
600			Power	Exhaust		
660		Exhaust				Power
720						

Table 2-11 Engine parameters for Ford V6 engine

Piston Bore	0.095504 m	Clearance length	1.27×10^{-2} m
RPM	2000	Compression ratio	10.5
Crank length to rod ratio	4	Atmospheric temperature	298 K

Figure 2-14, the discontinuity occurs due to the exhaust valve operation where the frequency depends on the engine RPM (2,000 in this case). The model reaches a steady-operation condition within two cycles of the engine. At the beginning of combustion, the concentration of HC is significant due to the injection of fuel, similarly the CO emission is high at initial firing due to insufficient air in cylinder during combustion. The NO

forms due to the temperature gradient and stabilizes as the system temperature gradient decreases. On the other hand, O_2 present due to the scavenging of cylinders and the pressure difference.

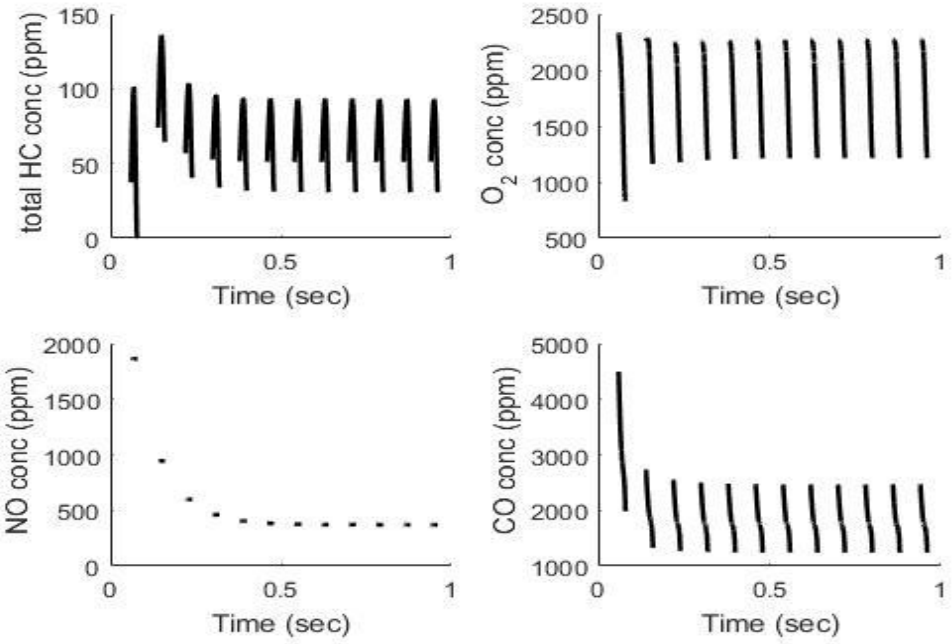

Figure 2-14 Out of cylinder emissions

2.6. **Engine Torque-Speed Model**

Governments test vehicles in a systematic pattern known as drive cycles such as the FTP-75, WLTC, and NEDC cycles. Major pollutants are formed during the cold-start and warm-up phases until a catalyst activation temperature is reached [40]. For a comprehensive simulation of emissions during realistic conditions, it is necessary to

include a speed-torque model, which computes the engine speed and load. The comprehensive emission model uses the EPA FTP-75 cycle for validations.

2.6.1. Background on Torque-Speed Models and Test Cycles

The driving cycles can divide into two major categories; legislative and non-legislative. Governments use the latter to measure emissions for legal certifications of vehicles. The primary purpose of the driving cycle is to represent actual driving conditions, which is presented by a speed-time profile corresponding to urban driving schemes. The driving cycles aim to relate the vehicle operating conditions with emissions. In modern days, the certification of new vehicles is subject to complying with the maximum emission standard outlined by various driving cycles. The driving cycles test various speeds, loads, and duration of the vehicle's operation.

In a vehicle, the engine management system (EMS) greatly influences the performance. The EMS divides into (1) AFR control, (2) Electronic throttle control (ETC), (3) Idle speed, (4) Ignition timing, (5) diagnostics, (6) turbocharger, (7) EGR, and (8) after treatment subsystems, which all contribute to the overall performance and emission quality. One of the most sensitive factors that concern drivers is the torque-speed demand of the vehicle, making it the cornerstone for engine development. Consequently, the need for detailed models that represents the vehicle's drivability leads the torque models to emerge.

Mapping-based approaches are among several methods to represent the torque-speed characteristics. For instance, Berglund [54] developed models using tabulated torque-speed data at steady-state conditions to predict the fuel economy through the

acceleration and load variation transient states. Rackmil et al. [55] utilized a correction factor to improve tabulated data methods to predict transient phases accurately. On the other hand, Jiang and van Gerpen [56] conducted a detailed analysis of transient behavior and cycle emissions using the FTP cycle but have only simulated the particulate matter. Similarly, Ericson et al. [57] studied all the pollutants of heavy-duty vehicles on the European test cycle. Giakoumis et al. [58] studied the NO and soot emissions for light and heavy-duty vehicles. Similar work studied engine soot emissions to develop a model for tip-in operations using empirical colorations [59]. Recent attempts by [60], [61] used neural networks for predicting transient emissions by utilizing steady-state emissions as training data.

A recent study [32], [58] developed an engine torque-speed model to relate engine torque-speed with emissions and predict emissions during transient stages. The experiments utilize an ultra-fast analyzer for NO and NOx measurements with a delay time of 2 ms. The model is based on steady-state measurements of engine and emissions to develop a quasi-steady map for emissions. Vehicle dynamics modeling helps in calculating the speed and torque of the engine. After completing the steady-state runs at the specified speed-load conditions, an engine map is developed to estimate various load-speed combinations. The overall empirical model is corrected using actual emission data during transient behavior.

2.6.2. Mathematical Model Development

The speed-torque model determines the engine torque requirements absorbed by vehicle resistance, acceleration, inertia, and other mechanical losses. The engine torque-speed

model converts the vehicle speed to engine RPM and torque. Figure 2-15 shows a schematic diagram of the engine-vehicle system modeled [62], [63].

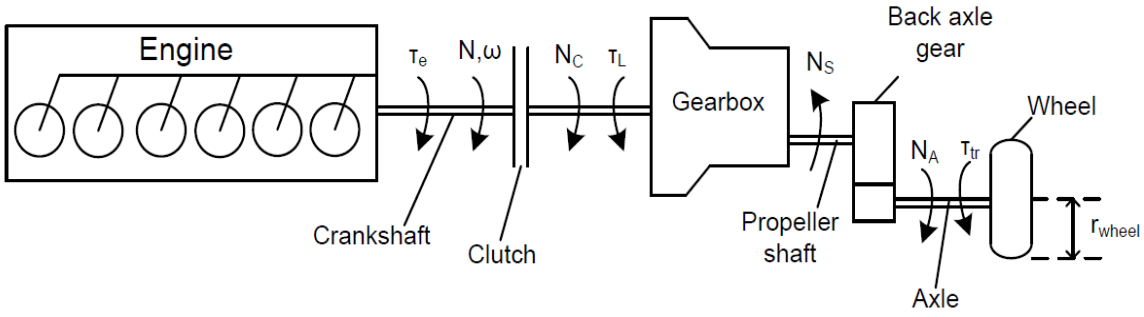

Figure 2-15 Vehicle propulsion system schematic

Applying Newton's second law of motion to the crankshaft results in:

$$\tau_e - \frac{\tau_L}{\eta_g} = \tau_A = G_v \frac{d\omega}{dt} \tag{44}$$

The model assumes that the rotating components, such as the gearbox, clutch, propeller shaft, and axle, contribute to the engine torque load [57]. Taking into consideration the gear efficiency and assuming an ideal operation of the gearbox, the model assumes the efficiency as $\eta_g = 0.96$. In the case where the engine is idle and no gear is engaged, equation 44 reduces to

$$\frac{\tau_L}{\eta_g} + G_v \frac{d\omega}{dt} = 0 \tag{45}$$

The ratio between the propeller shaft and the clutch gives the engaged ratio of the gearbox given by

$$i_g = \frac{N_c}{N_s} \tag{46}$$

Similarly, the rear axle ratio is defined by the rotational speeds of the propeller shaft over the drive axle speed:

$$i_b = \frac{N_s}{N_A} \tag{47}$$

Considering the various coupling and ratios of gears, the vehicle speed becomes

$$V\left(\frac{km}{h}\right) = 2\pi r_{wheel}\frac{N_c(RPM)}{i_g i_b} \times 60 \times 10^{-3} \tag{48}$$

Taking into consideration the various resistance forces acting on the vehicle, and by augmenting the forces into aerodynamic resistance, rolling resistance force, and the grade-dependent force, the total traction becomes:

$$F_{tr} = F_a + F_r + F_{gr} \tag{49}$$

The aerodynamic force as a function of densityρ_α, the frontal area A_f, drag-resistance c_d, and velocity V, is given by

$$F_a = \frac{1}{2}\rho_\alpha c_d A_f V^2 \tag{50}$$

The rolling resistance as a function of the vehicle mass, friction, and bearing friction is given by

$$F_r = m_v(f + c_{tr}V) \tag{51}$$

The traction torque is the total resistance force multiplied by the wheel radius,

$$\tau_{tr} = F_{tr} r_{wheel} \tag{52}$$

The total crack shaft axis torque as a function of the reduction ratios of the gears, back axle, and the resistance torque is:

$$\tau_L = \tau_{tr} \left(\frac{1}{i_b}\right)\left(\frac{1}{i_g}\right) \tag{53}$$

Given the various forces and inertias, the vehicle total moment of inertia is

$$G_v = m_v r_{wheel}^2 \left(\frac{1}{i_b}\right)^2 \left(\frac{1}{i_g}\right)^2 + G_e + G_x \tag{54}$$

Using equations derived above, the engine acceleration is

$$\frac{d\omega}{dt} = \frac{\tau_e - \dfrac{(\frac{1}{2}\rho_\alpha c_d A_f V^2 + m_v(f + c_{tr}V)) r_{wheel} \left(\frac{1}{i_b}\right)\left(\frac{1}{i_g}\right)}{\eta_g}}{m_v r_{wheel}^2 \left(\frac{1}{i_b}\right)^2 \left(\frac{1}{i_g}\right)^2 + G_e + G_x} \tag{55}$$

Given the relations derived by equations 44 to 55, the vehicle velocity-time data of the FTP-75 cycle data converts into engine RPM and torque data as a function of time. The vehicle's speed changes based on the throttle valve opening, allowing more air to flow and subsequently burning more fuel.

A throttle body model was proposed by [64] based on the throttle body diameter and runner diameter. The throttle model can be included in future work to act as the engine's initial input by providing the required air mass flow.

2.6.3. Torque Speed model Validation

The primary purpose of the torque-speed is to minimize the costs and provide a comprehensive model for estimating tailpipe emissions under realistic conditions. The

model is based on equations 44 to 55, derived in section 2.6.2. The model converts the vehicle velocity of the FTP-75 cycle (Figure 2-16) into engine RPM and torque data as a function of time. The speed-torque model calculates the engine torque requirements due to vehicle acceleration, resistance, inertia, and other mechanical losses. The model additionally calculates the vehicle rolling force, air resistance, and gear selection; shows typical FTP-75 cycle data.

Table 2-12 Test vehicle parameters

Mass of Vehicle	1500 kg	Gear Ratios	1^{st}: 5.78 2^{nd}: 2.70 3^{rd} : 1.90 4^{th} : 1.25 5^{th} : 1.00
Frontal Area	2.00 m^2		
Back Axle Ratio	2.70		
Wheel Radius	0.57 m		
Air Density	1.20 kg/m^3		
Front Axle to CG	1.95 m	Idle	1000 RPM
Front Axle to CG	1.30	Friction	0.057
Height of CG	0.89 m	Ge	0.87
C_r Rolling resistance	0.0015	G0	1.12

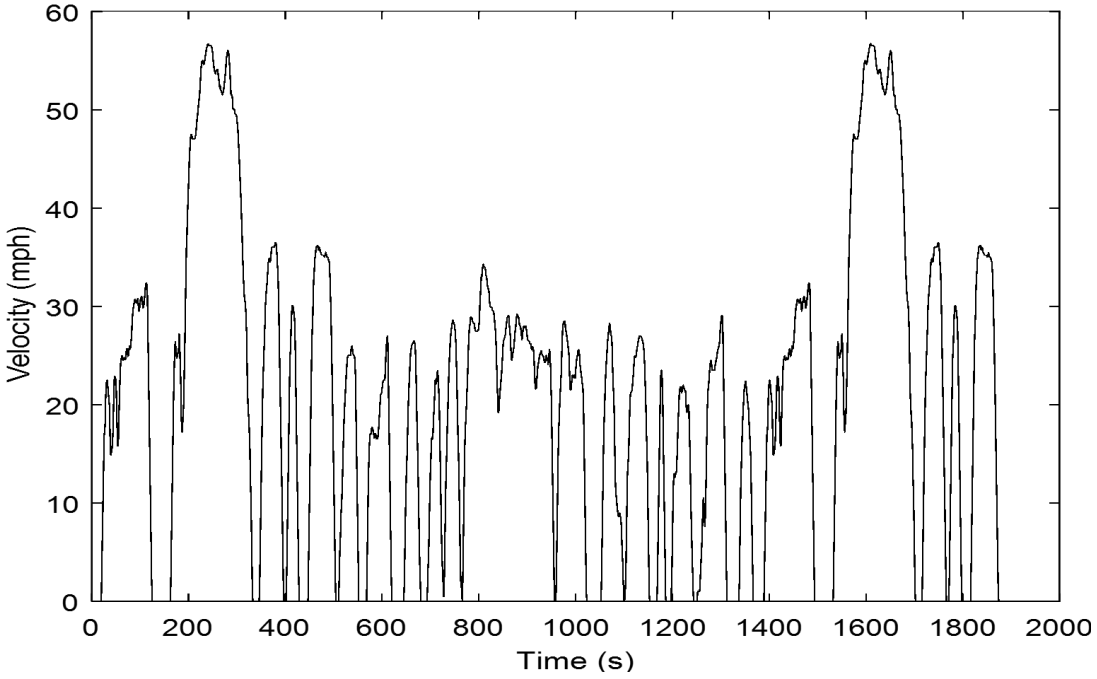

Figure 2-16 FTP-75 cycle

The calculated engine RPM and load depend on the vehicle under study, resistance, and gear ratios, as in Table 2-12. The engine speed variations between 1,600 to 2,100 RPM (Figure 2-17) reflects the acceleration and torque requirements. The discontinuities in torque (Figure 2-18) occurs when engine is disengaged during shifting. Figure 2-19 shows aerodynamic resistances, which is a function of the vehicle speed and frontal area. Figure 2-20 shows the gear shifting action, which depends on both the RPM and torque required.

The actual load and speed vary depending on the driver's shifting between gears. The simulation model data utilizes the recommended ideal shifting schemes by the

vehicle manufacturer. A 10-15% margin of error can account for the discrepancies between actual driving styles and the ideal theoretical data.

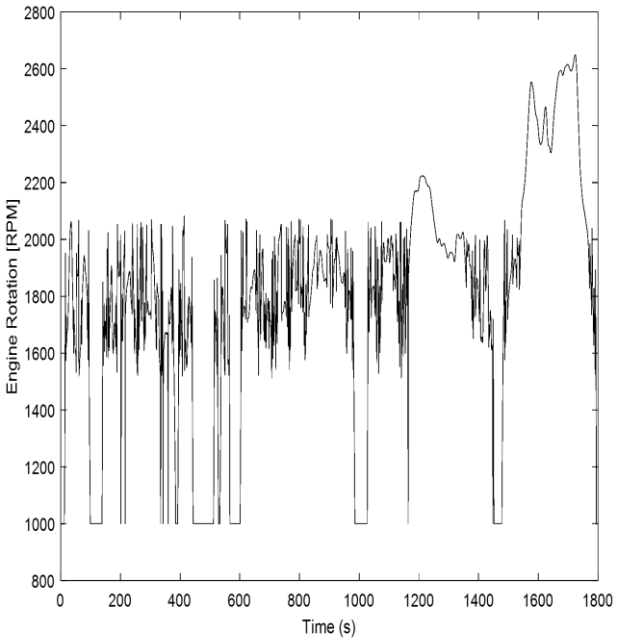

Figure 2-17 Engine RPM during the FTP-75 cycle

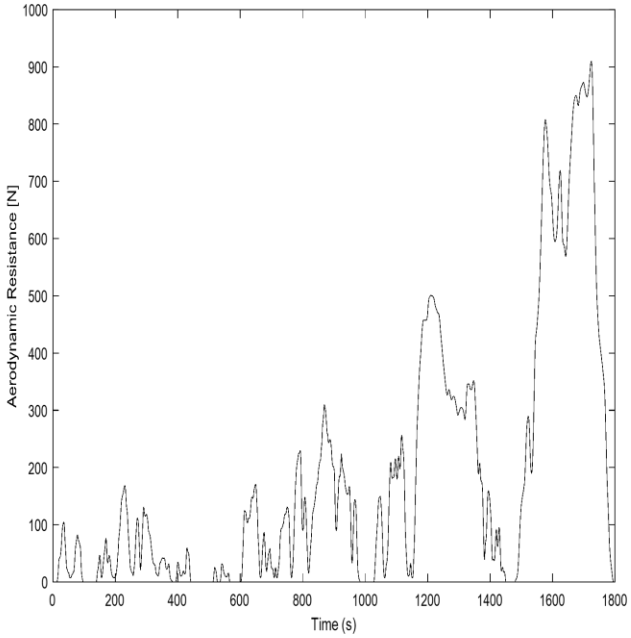

Figure 2-18 Aerodynamic resistance during the FTP-75 cycle

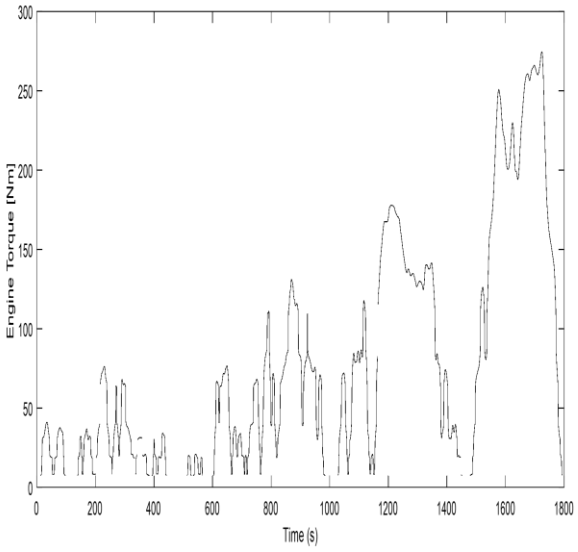

Figure 2-19 Engine load during the FTP-75 cycle

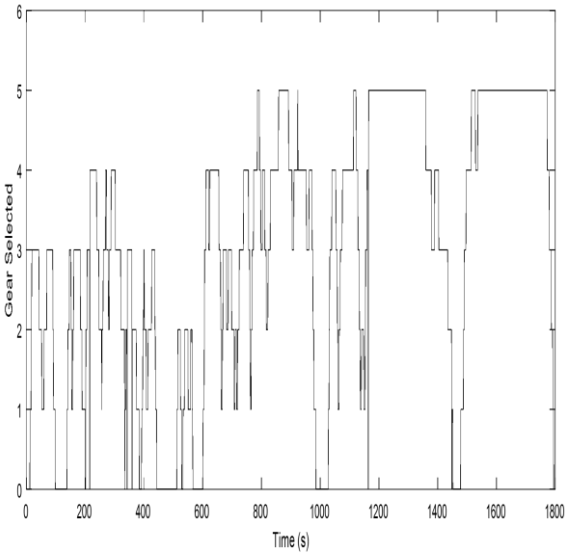

Figure 2-20 Gear Selection during the FTP-75 cycle

3. INTEGRATED MODEL RESULTS AND DISCUSSIONS

The overall aim is to achieve an integration prediction criterion for tailpipe emission from a multi-cylinder SI engine. The interaction between components is complex and the transient representation requires well established temporal representation. The modeling efforts for representing the interactions during drive cycles and real world can be divided into three main categories: physics-based modeling, empirical representation, and machine learning algorithms.

Empirical emissions models such as [65]–[69] are specific to the studied condition, and extrapolating the model predictions for drive cycle prediction results in significant errors. Recent developments in machine learning such as [70]–[73] allows exploring the emissions from engine under different operating conditions, however the accuracy depends on the measurements used for the model development.

Physics-based emission models include multiple vehicle components such as combustion, manifolds, catalytic reduction technologies, drive. Many studies [74]–[77] use a comprehensive CFD analysis approach of components, which requires advanced computing devices for efficient representation. Alternatively, lower-order models such as [78]–[80] use heat models, mean value models, and sub-modeling approaches in representing the real-world driving emissions. The latter approach presents a viable methodology for modeling emissions for different operating conditions and provides high accuracy.

The model presented here follows an integration methodology based on co-simulation framework such as that presented by [81]–[83] but includes the three-validated mentioned vehicle components. The two main tasks include:

1- Emission Model: Develop an emission mathematical model consisting of combustion and after-treatment system (Engine-Exhaust-TWC).

2- Integrated Model: Develop a torque-speed integrated model based on an FTP-75 test cycle.

The first task composes of appropriately integrating an SI engine model, with the exhaust manifold, and finally incorporating the TWC model to estimate tailpipe emissions. The second task focuses on integrating the torque--speed model with the vehicular components in the first task. The integrated model is used to predict the transient emissions during the FTP-75 cycle. The combustion model uses the driving cycle data presented by RPM and load as input. Figure 3-1 shows the dependency of tasks to achieve a complete representation of emission prediction during the entire drive cycle.

The preliminary evaluations of vehicle emissions using computer models reduce testing costs and preserve natural resources. Thus, converting the vehicle's velocity into engine torque and RPM is necessary to estimate the emissions. The model utilizes the vehicle inertia, resistances, and propulsion requirements to a set of engine RPMs and load data. At the lab, a dynamometer resembles the loads encountered by the vehicle during acceleration, deceleration, and coasting through applying the load to the engine.

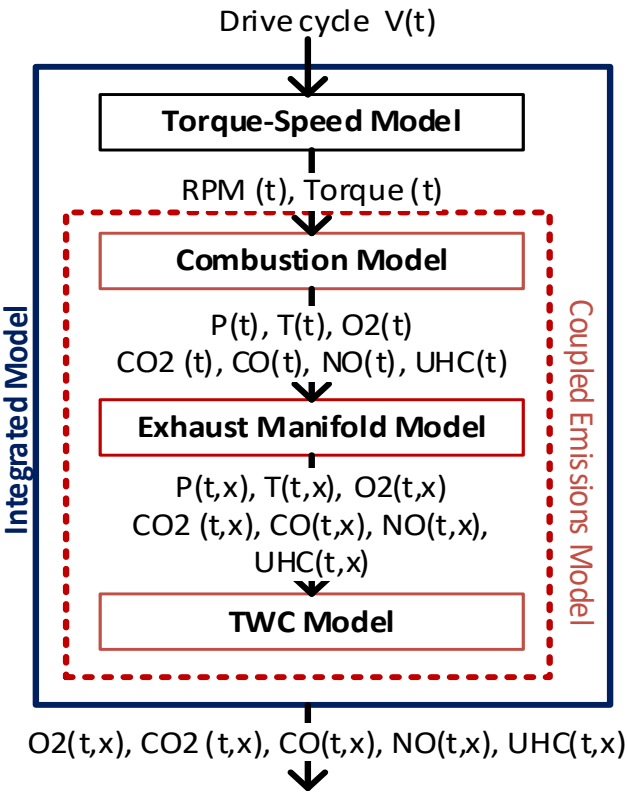

Figure 3-1 Model development process

3.1. **Emission coupled model validation**

Exhaust gas dynamics interconnect the engine and TWC through the exhaust manifold. For combustion, the in-cylinder exhaust properties such as pressure, velocity, and temperature are the initial conditions for the exhaust manifold. Similarly, the exhaust manifold model provides the initial conditions for the TWC model.

In combination with the combustion and TWC models, the exhaust manifold provides a comprehensive model for predicting the tailpipe emission of an SI engine. The coupled emission model is calculated a full load criterion (Wide Open Throttle,

WOT). Simulations were performed using Matlab software installed on a 64-bit Windows 7 operating system. The PC had an Intel Core i7-4700 rated at @3.40Ghz and 8GB RAM.

For simulations, the manifold has a length of 0.5 m and cast iron as a material. The model predicts the instantaneous emission properties such as pressure, velocity, density, and temperature. The model assumes no reaction for the emission species along the manifold. Thus, the exhaust model acts like an accumulator based on the conservation equations. Figure 3-2 compares the calculated and measured exhaust pressure at 2,500 RPM and WOT conditions. The pressure upstream of the TWC with a maximum of 1.24 bars and a minimum of 0.95 bars experimentally, while using LW2 show a maximum of 1.25 bars and a minimum of 0.98 bars, with a percentage difference of 3%. The pressure drop occurs due to pressure waves traveling pulse creating a negative pressure. The pressure behavior allows the full evacuation of the gas in the cylinder and improves the engine's volumetric efficiency.

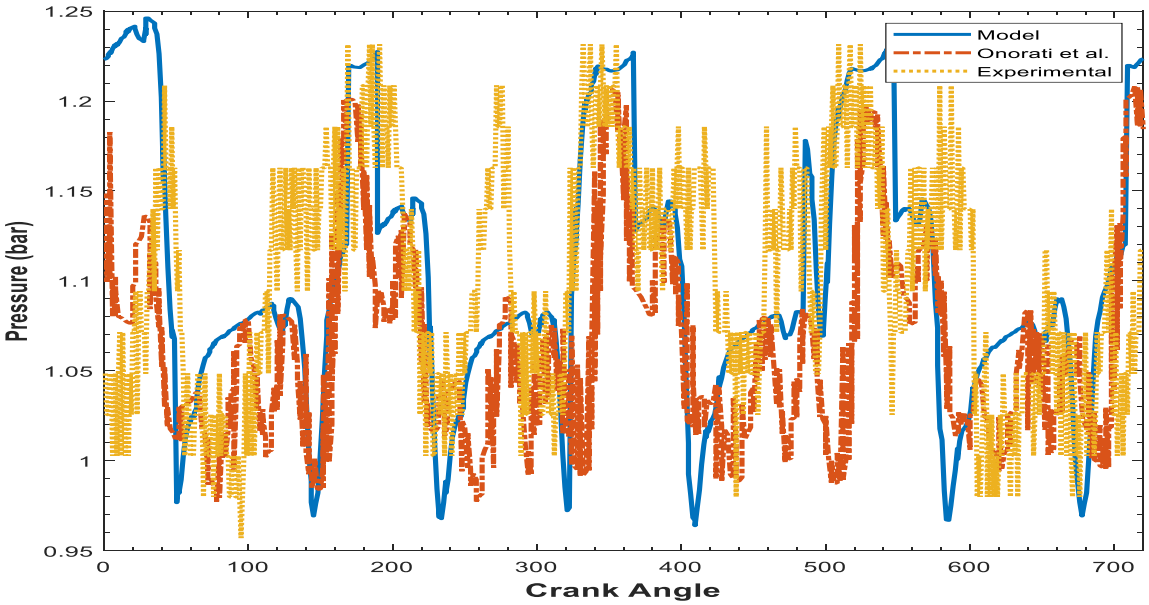

Fig. 3-2 Experimental model validation of the exhaust gas manifold at 2,500 RPM

The model shows a sudden increase in the pressure at 60° and a relatively smoother region at the end of the power stroke at 120°. The smoother region shows a secondary increase in the pressure between 100° and 120°, which is due to the extraction dynamics of the cylinder during the exhaust stroke and the valve dynamics.

The valve opens based on the overhead cam profile during the exhaust stroke, which shows a parabolic profile. The minimum pressure at the exhaust manifold happens when the valve is closing. Figure 3-4 shows a typical lift profile of exhaust and intake cam, when the valve is fully opened the flow rate is maximum. The duration when the valve is open results in higher pressure values and a smoother pressure change, as modeled in Figure 3-3.

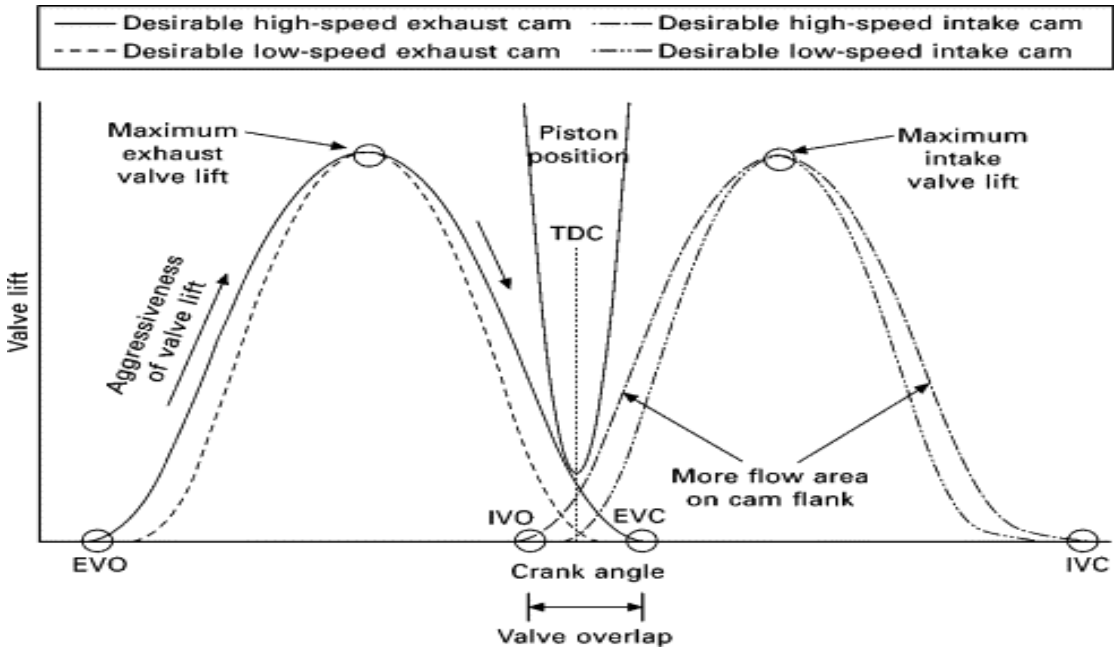

Figure 3-3 Exhaust valve opening profile [85]

The developed model predicts the pressure peak values with an average error between 1% and 7%. The differences are mainly due to the solution methods implemented for the exhaust manifold. Onorati et al. use the modern characteristic-element-solution element (CE-SE) to solve the system. The waves at 120° multiples represent the phase difference between the V6 engine cylinders (following a 142536-firing order). The model can predict abrupt pressure changes effectively at the steady operation, as shown by the peaks at 180˚, 360˚, and 540˚. The model prediction aligns with the CE-SE results by Onorati et al. [65] for the evaluated operating conditions.

Comparing the complexity of both methods, the LW2 is efficient compared to the CE-SE method.

Figure 3-4 shows the predicted gas pressure at the exhaust manifold upstream of the TWC at 1,500 RPM and 90% load. Figure 3-5 shows the system reaches a steady-operation condition within 0.05s, which is the time required for a complete engine cycle. The system shows an irregular pulse between 0-0.05 s, the duration of which the exhaust valve is open. The initial model conditions dictate the system condition before the exhaust pulse, imposed by the exhaust gases entering the exhaust manifold. The consequent initial conditions in the manifold use the end conditions of the previous time. Thus the system pressure, velocity, and density change until it reaches a steady-state operation. The initial conditions are the atmospheric conditions, i.e., 0 m/s, 1.2 kg/m^3, and 1 bar for velocity, density, and pressure, respectively.

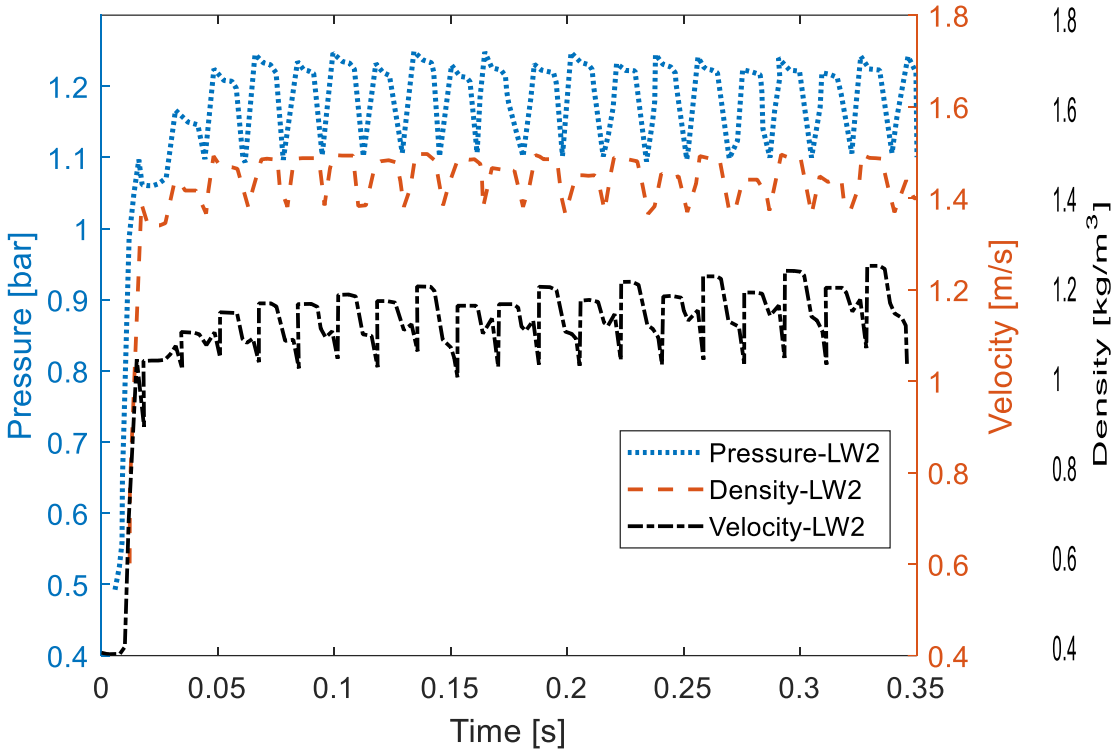

Figure 3-4 Manifold exhaust gas pressure, density, velocity at 1500 RPM, and 90% load

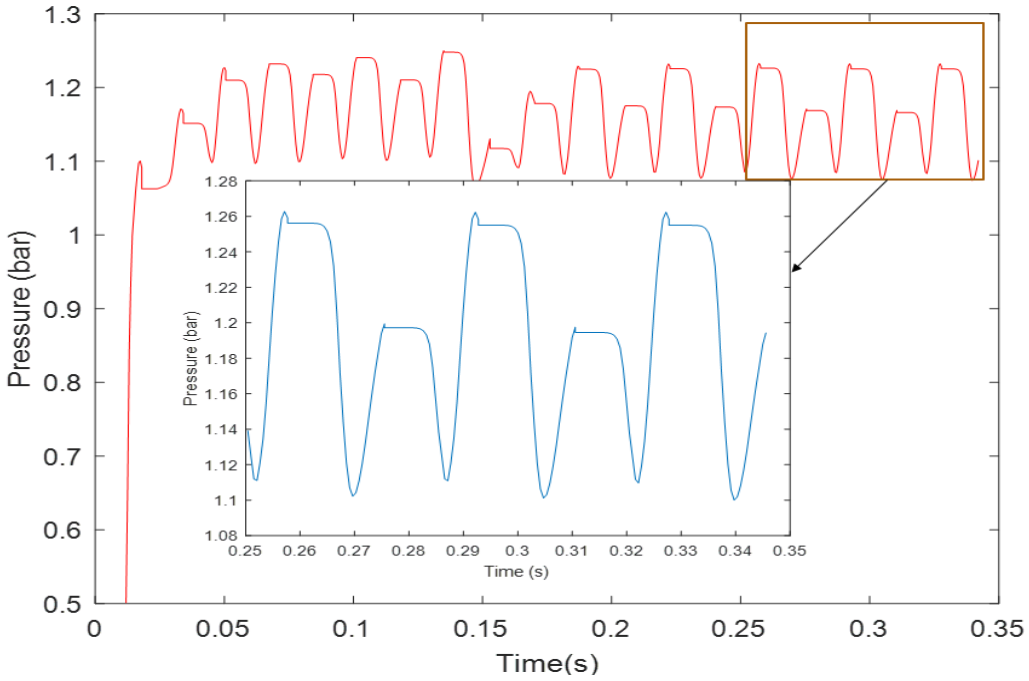

Figure 3-5 Manifold exhaust gas pressure at 1500 RPM and 90% load

Figure 3-6 shows experimental validation for the exhaust manifold model evaluated at 2,000 RPM and full load. Experimental validation shows that model results agree with experimental values. The model maximum and minimum values of 1.41 and 1.32 bars match with measured experimental results. However, the theoretical model underpredicts the effect of secondary waves in the exhaust manifold due to the pulse effect based on the firing order of the multi-cylinder engine. The secondary wave is due to the effect of subsequent cylinders with a phase angle of 120°. The exhaust pressure is based on the left bank only, hence, a 240° shift is realized. The effect of the secondary wave is underestimated, with a percentage difference of 2% at 2,000 RPM; the model minimum values prediction of 1.34 compared to 1.32 bar measured experimentally. However, the matched data presents a good agreement; the experimental data shows high sensitivity to any slight variation in the engine speed. For theoretical model data, a similar sensitivity was not realized, where the theoretical model was more stable due to the steady-state architecture of the model.

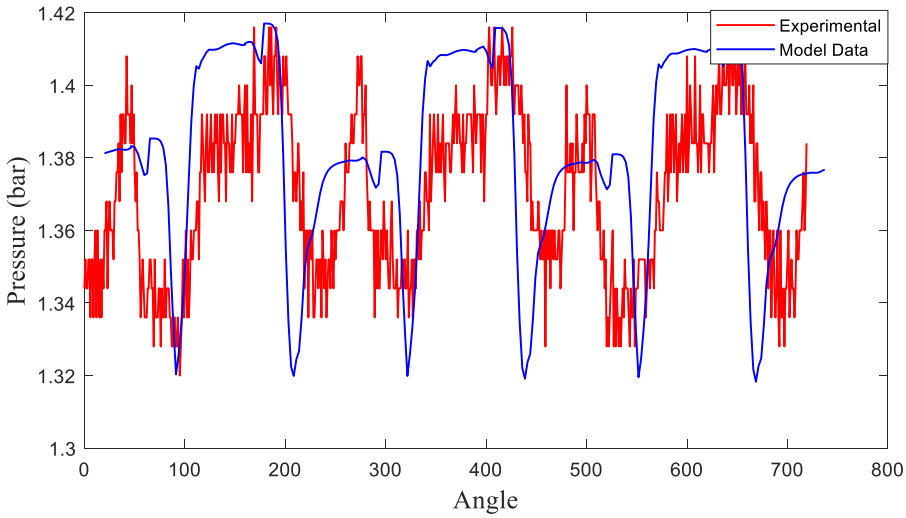

Figure 3-6 Experimental vs. theoretical exhaust manifold pressure at 2,000 RPM

The pulsating behavior is crucial for the TWC model's effectiveness and accuracy due to its effect on the absorption and adsorptions at the catalyst surface [34]. Additionally, accurate prediction is essential to TWC design optimization and emission predictions during cold start and determining the light-off duration for the TWC. In general, the presented model can estimate the exhaust gas properties at both temporal and spatial variations of the exhaust manifold geometry. The use of exhaust manifold shows the variation of exhaust gases and the need for updating TWC and emission models to incorporate the pulsation effect, which subsequently improves integrated emission models.

The experimental validation of both the exhaust manifold and coupled models relies on 24 measurements. These measurements consist of four speeds: 1,000, 1,500,

2,000, and 2,500 RPM, and six loads 0%, 20%, 40%, 60%, 80%, and 100% for each speed. Figures 3-7 and 3-8 show the engine characterization by representing the load percentage based on the Inlet Manifold Pressure (IMP), torque, and power. In the following analysis, IMP reflects the load, where 0 atm IMP is a full-load condition a full load map is provided in Figure 3-7 and 3-8.

Figure 3-9 shows the engine torque and power measurements conducted at 1,000 RPM, which shows the transient overshoots for both torque and power. The overshoot is due to the increase in the load applied by the dynamometer on the engine. Thus, to minimize transient error and ensure steady-operation measurements, for each engine speed run, the system records emissions for 60 seconds in steady-state and allows transient measurements for an additional 120s between each load increase. The data shows slight fluctuations in the torque and power values due to the instability and slight engine speed changes. Several aspects contributed to uncontrolled engine speed fluctuations, including fuel pump, fuel injector, spark plug, and water flow into the dynamometer. The fluctuations can be eliminated computationally using data filtering techniques; however, filtering was not implemented in the current study to ensure the accurate representation of data. Table 3-1 shows the conversion factors used to present the exhaust gases CO, CO_2, NO_x, O_2 as mole fractions.

Table 3-1 Emission conversion factors

CO	*CO_2*	*O_2*	*NO*
100%	*Maximum*	*Maximum*	*100%*
4750 ppm	19%	22.5%	5000 ppm

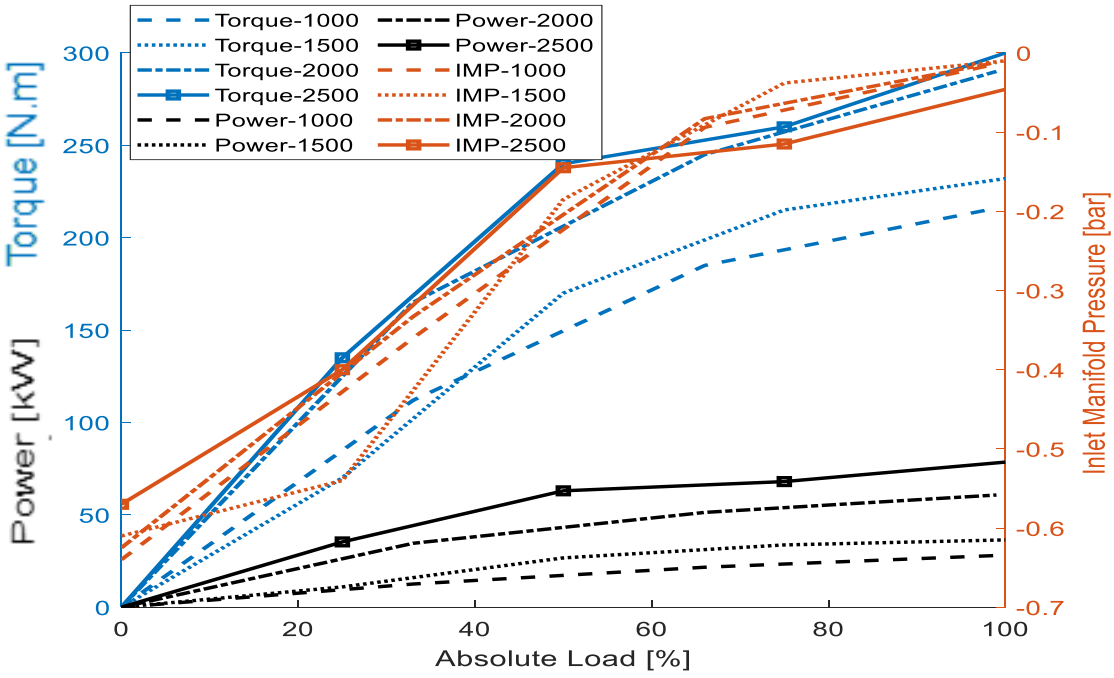

Figure 3-7 Engine-performance at different testing loads

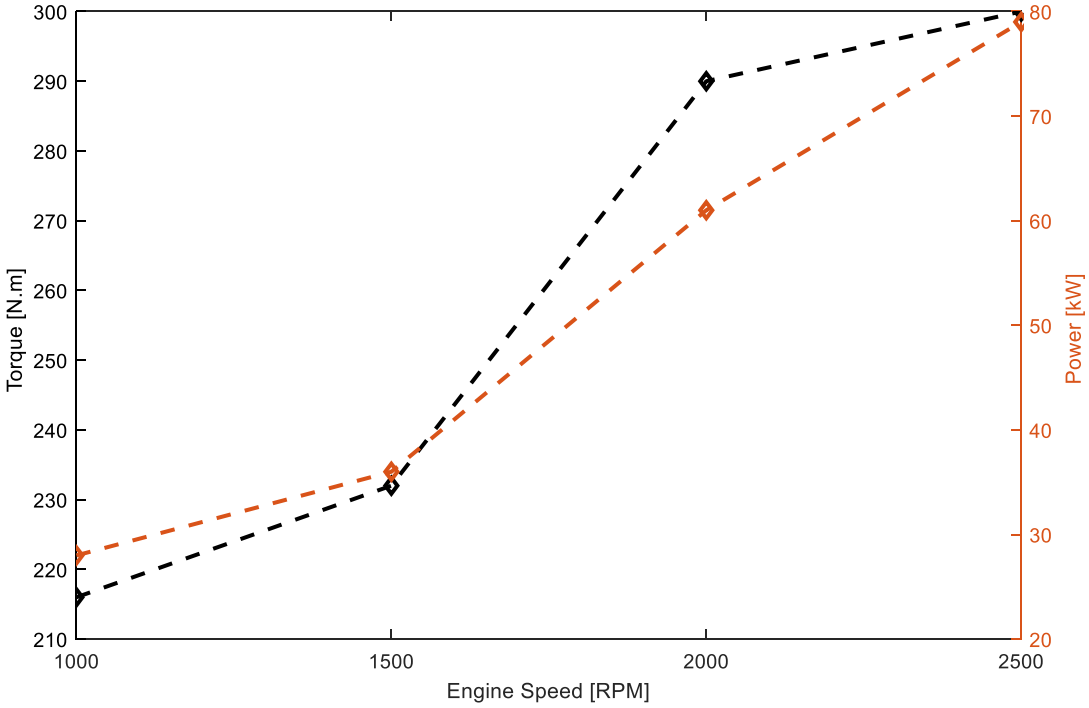

Figure 3-8 Engine performance curve WOT

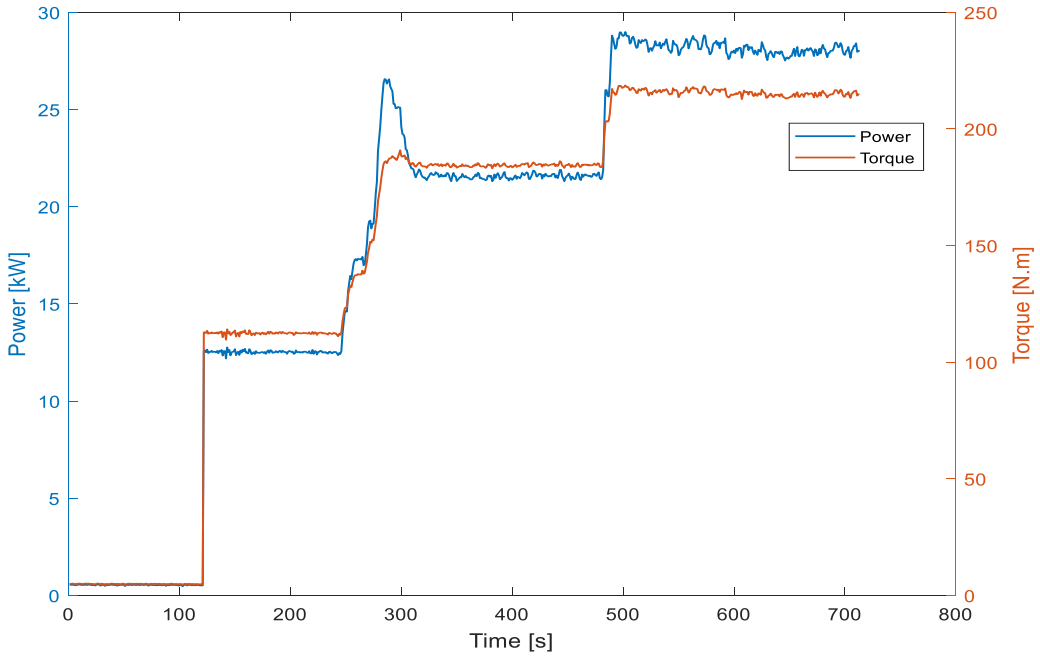

Figure 3-9 Experimental engine power and torque at 1,000 RPM

The exhaust manifold model developed in section 2.3 is coupled with Kumar's improved low-order combustion model section 2.5 [52]. The combustion model considers two-gasoline fuel species made up of 80% fast-burning fuel (iso-octane) and 20% slow-burning fuel. Adjusting the fuel ratios minimizes experimental error deviations because of actual fuel inconsistencies.

The relatively low exhaust gas reactivity in the exhaust manifold compared to the reactivity at the TWC allows pure species transport from the engine block to downstream components; consequently, the species at the manifold is only based on the conservation equations. Accordingly, as described by (15a) and 15b), the combustion model output (temperature, pressure, gas compositions) is set as the exhaust manifold's boundary conditions. A similar application of boundary conditions coupling was used in Olczyk [86] to estimate the properties of a pulsating flow (pressure, density, and temperature), correspondingly using a second-order FDM to discretize the computational grid.

Figures 3-10 to 3-14 show the experimental and integrated model emissions for individual species at wide range of running conditions. Generally, theoretical and experimental data match with a maximum error of 50% and a minimum error of 10%.

O_2 emission: Figure 3-10 shows the measured and predicted out-of-cylinder oxygen concentration. At all engine speeds, increasing the engine speed at 0% load does not affect the oxygen present in the exhaust gases (stays around 5% for all RPMs). However, increasing the load from 0% decreases the concentration from 5% to 1.5%. Higher loads require more fuel and oxygen, resulting in the exhaust’s reduced oxygen

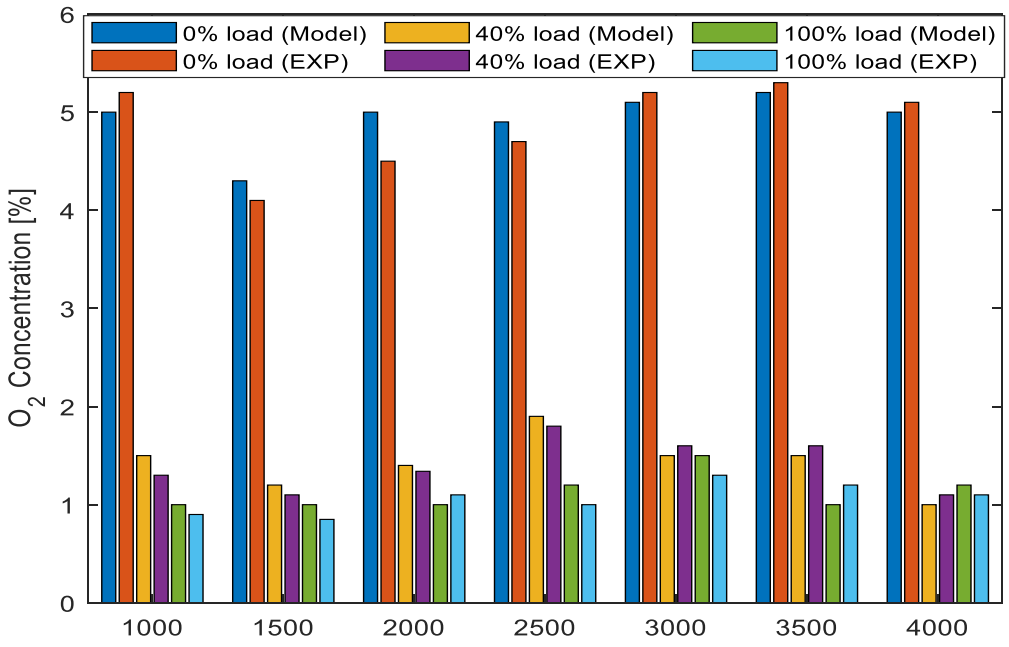

Figure 3-10 O_2 Engine emission at typical operating conditions

content as the load increases. On the other hand, at lean-fuel conditions such as 0% load, a high AFR results in higher oxygen in the exhaust. Comparing the model with experiments shows errors as low as 3% at a wide range of operating conditions but increases slightly for a full load to 11%. Generally, the model aligns with the experimental study within an average of 7%.

CO_2 emission: Figure 3-11 shows the CO_2 measured and predicted out-of-cylinder concentration. At 1,000 RPM, by increasing the load from 0% to 40%, the CO_2 increases by around 120%; however, by increasing the load to 100%, CO starts forming, and the CO_2 increases by only 20%. At 0% load, the amount of fuel is low compared to full load, thus lowering the CO_2. Below 3,000 RPM, the 40% load CO_2 is the highest

due to the complete combustion. The prediction error averages 10% for most operating conditions and further declines at high load and speed to 5%.

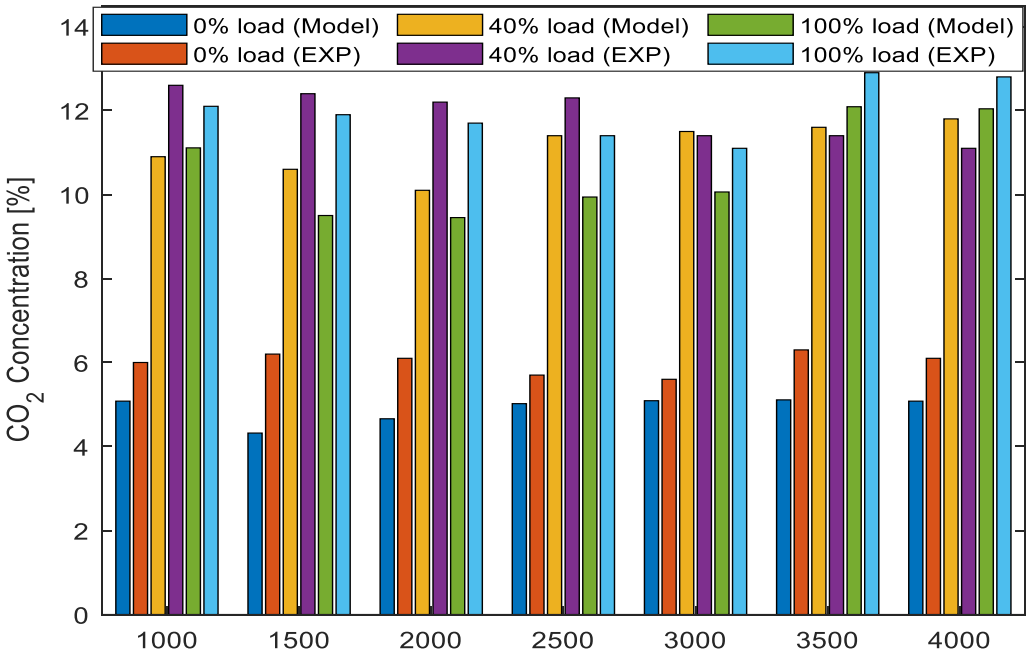

Figure 3-11 CO_2 emissions at typical engine operating conditions

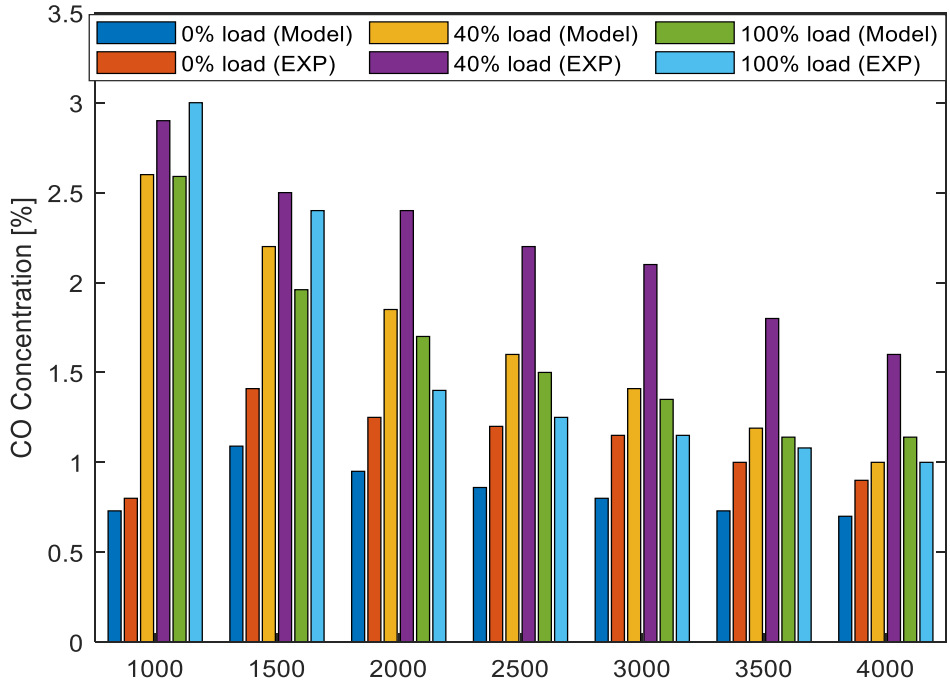

Figure 3-12 CO emissions at typical engine operating conditions

CO emission: Figure 3-12 shows the measured and predicted CO emissions. Increasing the speed reduces the CO while increasing the load increases the CO concentration. The behavior is affected by the fuel and burn effectiveness, where emission is the lowest at higher speed and low load. The resistance on the crankshaft at a high load disturbs the movement of the piston, consequently the combustion and emissions. Overall, the model performs well at 0% and 100% load, with a maximum error of 5%, while increasing for the mid-load range.

NO emission: Figure 3-13 shows the measured and predicted NO emissions. Increasing the speed at full load decreases the emission formation by around 35% but rises by approximately 20% for 4000 RPM. Increasing the load from 0% to 100% results

in 600% emission increases; for instance, at 3000 RPM, the concentration increases from 50 ppm at 0% load to 800 ppm at 40% load. Temperature is the main factor influencing the NO and CO formation; based on thermodynamics' first law, increasing pressure and temperature yields higher power output, helping NO formation. Similarly, increasing the fuel input at high loads increases the in-cylinder temperatures and consequently forms NO and CO. Experimentally, the error is as low as 6% at most operating conditions but higher at a few instances. Generally, the increase of engine speed at lower loads does not affect the concentration, stays below 100 ppm, and shows a minimum of 6% error.

UHC emission: Figure 3-14 shows the measured and predicted UHC emission. The UHC is the highest at 0% load due to the low inlet air into the cylinders and high fuel level. At 100% load, UHC concentration is similar to 40% load due to higher AFR. Experimental results are consistent with theoretical predictions at most operating conditions but deviate at 0% load. The difference between model and experimental results ranges between 1% to 3% for loading conditions but becomes significant at 0% load. The testing equipment influences the error at 0% load and results in an unusually high emission value.

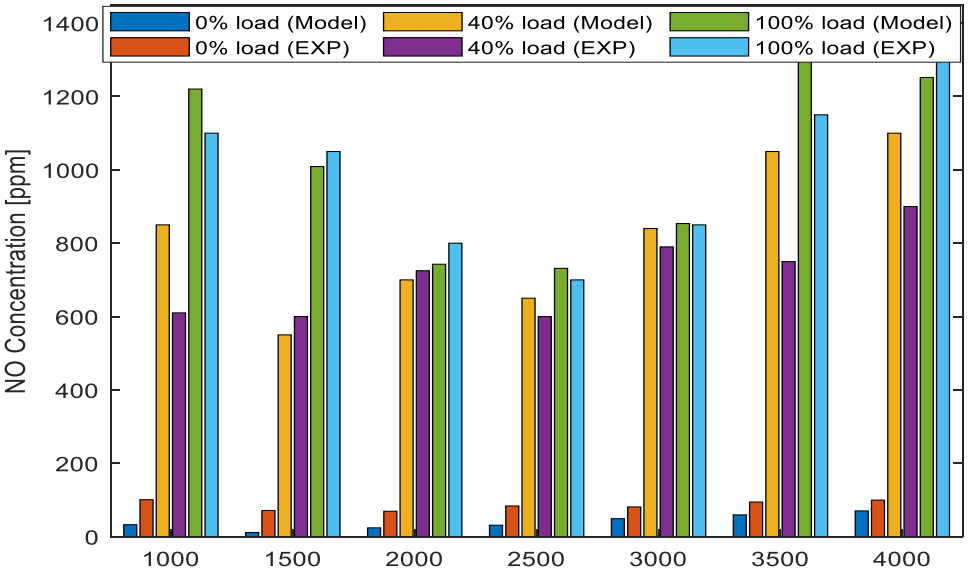

Figure 3-13 NO emissions at operating conditions

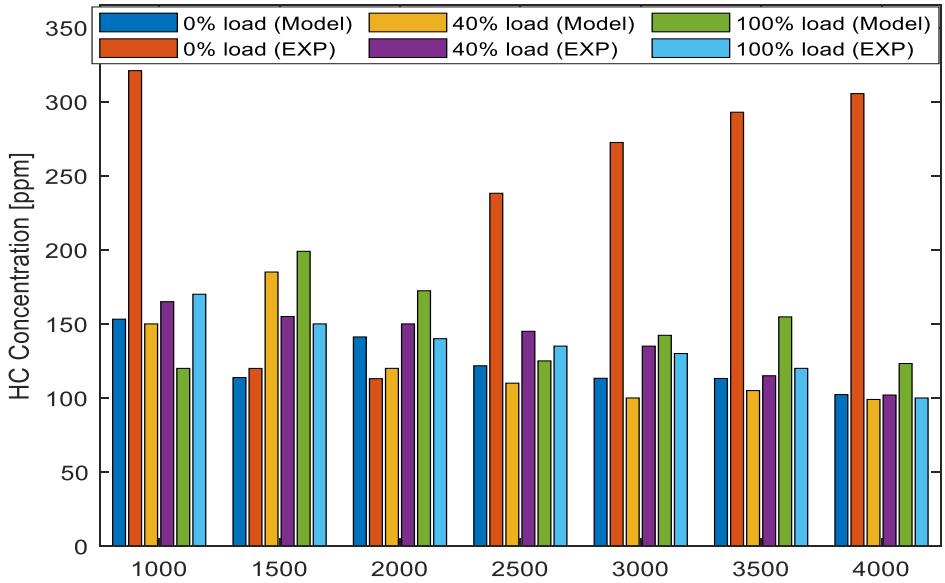

Figure 3-14 UHC emissions at operating conditions

The emission model assumes air and fuel to be premixed before injection into the cylinder. In experiments, the fuel is injected into the cylinder and then it mixes with air during the intake stroke. Additionally, the spark in the theoretical model supplies constant energy to the cylinder. On the other hand, experimentally, the fuel burns in waves known as wave fronts, creating multiple power incidents in the cylinders. The engine used for experiments uses spark advance timing, which is not included in the current theoretical work. Also, the engine fueling is aspired by spark advance and retard timing, affecting the temperature inside the cylinder and consequently the emission formation. Therefore, any variations in the spark efficiency at the cylinder would mainly affect the CO and CO_2 emissions. The theoretical model accounts for this indirectly through mixing times, which in the experimental case presents the wave propagation of the flame front after the ignition of the fuel-air mixture. The theoretical model assumes a two species gasoline mixture consisting of 80% fast-burning gasoline and 20% slow-burning gasoline. The fast-burning gasoline presents isooctane, while the slow-burning gasoline presents the hydrogen ratio of actual gasoline. The gasoline used for the experiments was locally acquired, and chemical data sheets are not readily available. Based on that, an assumption on the fuel composition was made, which adds to the inaccuracy of the experimental work.

The model shows to be more accurate with the significantly reduced error between the comprehensive model and experimental results. The differences are due to the low-order assumption used for the theoretical model. The variation in results does not owe to the difference in theoretical model architecture only. Still, various factors that

affect the experimental results' accuracy were not included, such as the compression ratio, fuel used, octane number, spark plugs conditions, and carbon built up in the cylinder. The accuracy of the current experimental setup could be improved by including additional measurements of crank angle, in-cylinder temperature, and heat transfer rates. Initial attempts use AVL Indicom DAQ to measure the crank angle and spark timing experimentally; however, due to the complexity it imposes on the theoretical model, these interactions were not included in the present work.

3.2. **Integrated Model Validation**

In this section, the torque-speed model (section 2.6) is implemented using the FTP-75 cycle data. Figure 3-15 shows the RPM and torque (equations 44-55) for a test vehicle with parameters shown in Table 2-12. During gear changes, the clutch disengages, and no load is transferred, resulting in zero torque. The idling engine speed is set to 800 RPM accounting for the accessories, such as the alternator and AC compressor. The integration of the torque-speed model allows quantifying the emission through inclusion of the vehicle characteristics such as gear ratios, frontal area, and inertia.

The TWC model calculates the tailpipe emissions based on cycle input. Figure 3-16 shows the results for 1,500 RPM at partial load conditions. The emission input from the combustion model transfers via the exhaust manifold for reduction via the TWC. The emission prediction is 10-22% lower than the experimentally measured emissions.

The improved TWC model incorporates platinum group metals (PGM) to reduce CO, H_2, HC, and NO_x. The cerium medium stores oxygen during lean periods and

reduces emissions during the fuel-rich periods. The reactions over PGM are much faster than the surface storage reactions. Thus, the reactions over PGM acts as global reactions ignoring surface storage. The surface reaction assumption referring to the adsorption and desorption reactions over PGM are swift and do not need to be explicitly modeled.

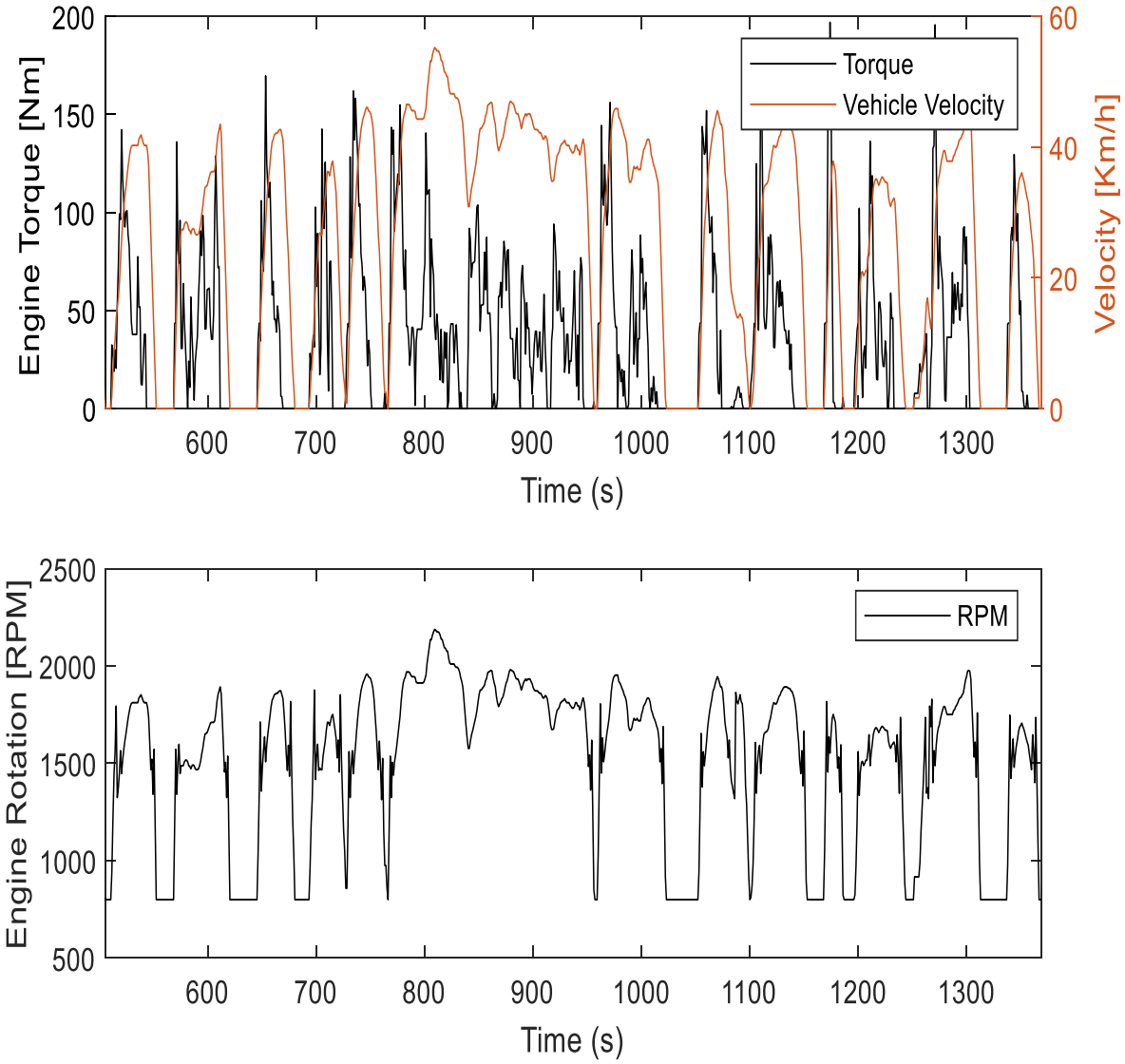

Figure 3-15 Transformed vehicle speed to the engine RPM and torque during an FTP-75 cycle

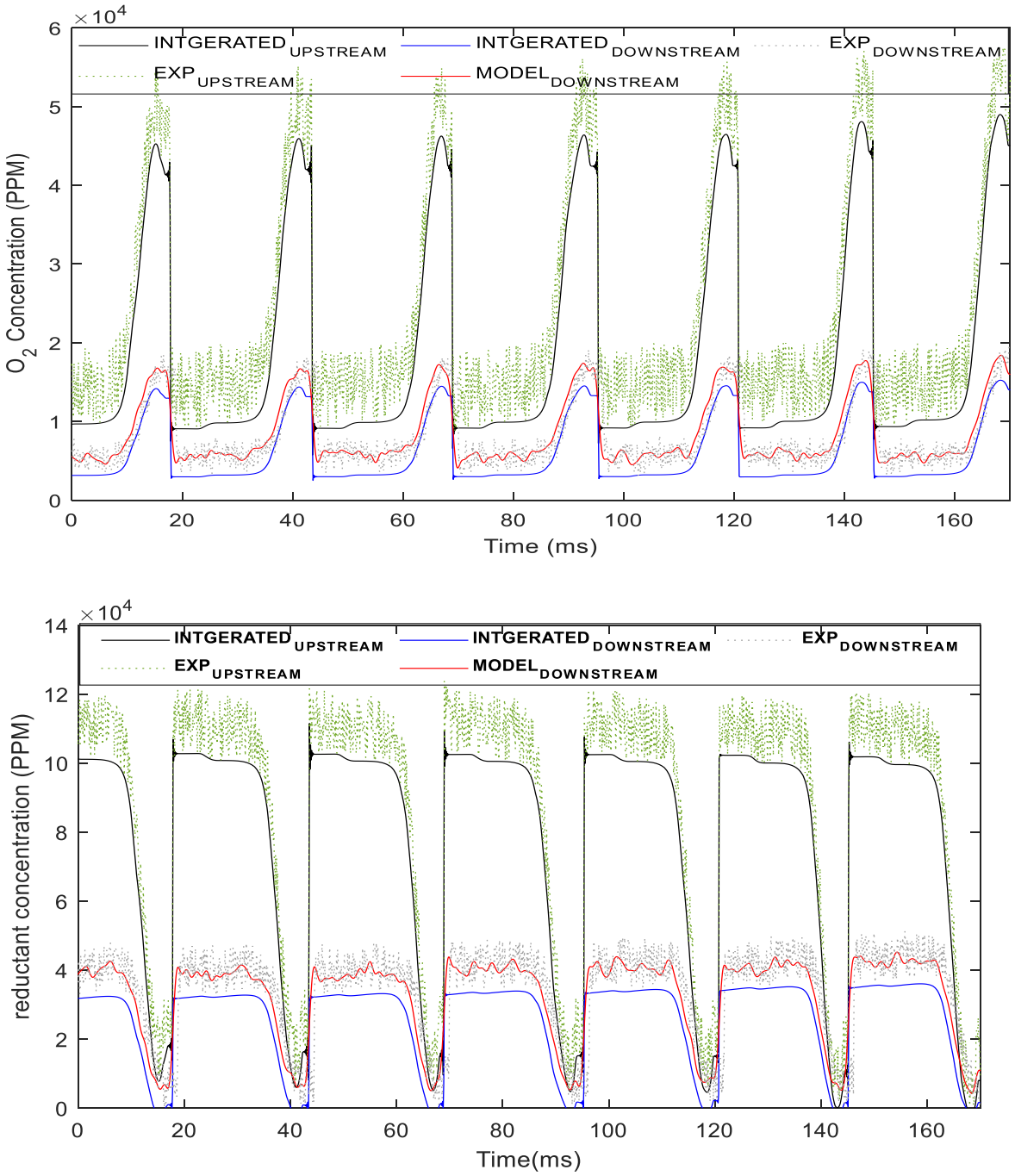

Figure 3-16 Emissions at 1500 RPM and partial load, exhaust manifold model (black) overlaid with the experimental emission upstream (green), downstream

3.3. **Transient Model**

The integrated model predicts transient emissions by integrating two models: (1) torque-speed model (Section 2.6), with (2) the coupled emissions (Sections 2.3-2.5). Transient emission prediction for drive cycles such as FTP-75, NEDC, WLTC is based on applying the instantaneous speed and load data, predicting the formation during acceleration and deceleration phases.

Figure 3-18 shows the emission prediction during an FTP-75 cycle using the integrated model. The results show that the acceleration period imposes rich conditions at the cylinder, resulting in decreased oxygen (blue) and increases the reductant emissions such as CO, HC, and NO (red). For instance, during the first 200 seconds, the reducing agent emissions instance (calculated for each engine cycle) changes between 0-14 g/s under accelerating conditions. However, the oxygen formation does not exceed 4 g/s even during deceleration when the engine runs lean. The deficiency in oxygen formation in the exhaust gases is due to the TWC storage mechanisms during lean conditions. The storage capacity and release of oxygen are reflected between 100-200 seconds, where the emission formation does not exceed 7 g/s even though the vehicle is under acceleration. Between 180-200 seconds, the car reaches a stop, and the oxygen formation increases after filling the oxygen storage. Analogous filling and emptying events occur during the various phases of the drive cycle. The quantification of oxygen concentration allows studying the oxygen storage during lean periods, which reduces the reductants emissions during the rich periods and explores the possibility of lean-operation engine development.

The integrated model time steps depend on the engine cycle duration (for example, at 1,500 RPM, the emission instance is every 0.08s). This can help accurately predict each cycle's effect on the emissions formation. Comparing the developed model with industrial standards such as *ADVISOR* [87], which uses a fixed calculation rate for the emissions, shows that the model varying time step approach is capable of calculating the instantaneous emissions with high resolution that depends on the operating conditions.

Most transient models heavily depend on steady-state engine operation to create transient maps and model adaptation methods. This technique requires creating lookup tables for emissions and extensive experimental efforts. The steady-operation tests do not correctly capture the transient effects during acceleration and do not reflect TWC oxygen storage capacity. As shown in previous sections, the developed integrated model provides high accuracy data in line with real-world measurements while offering a fully integrated analysis of combustion, exhaust manifold, and TWC systems.

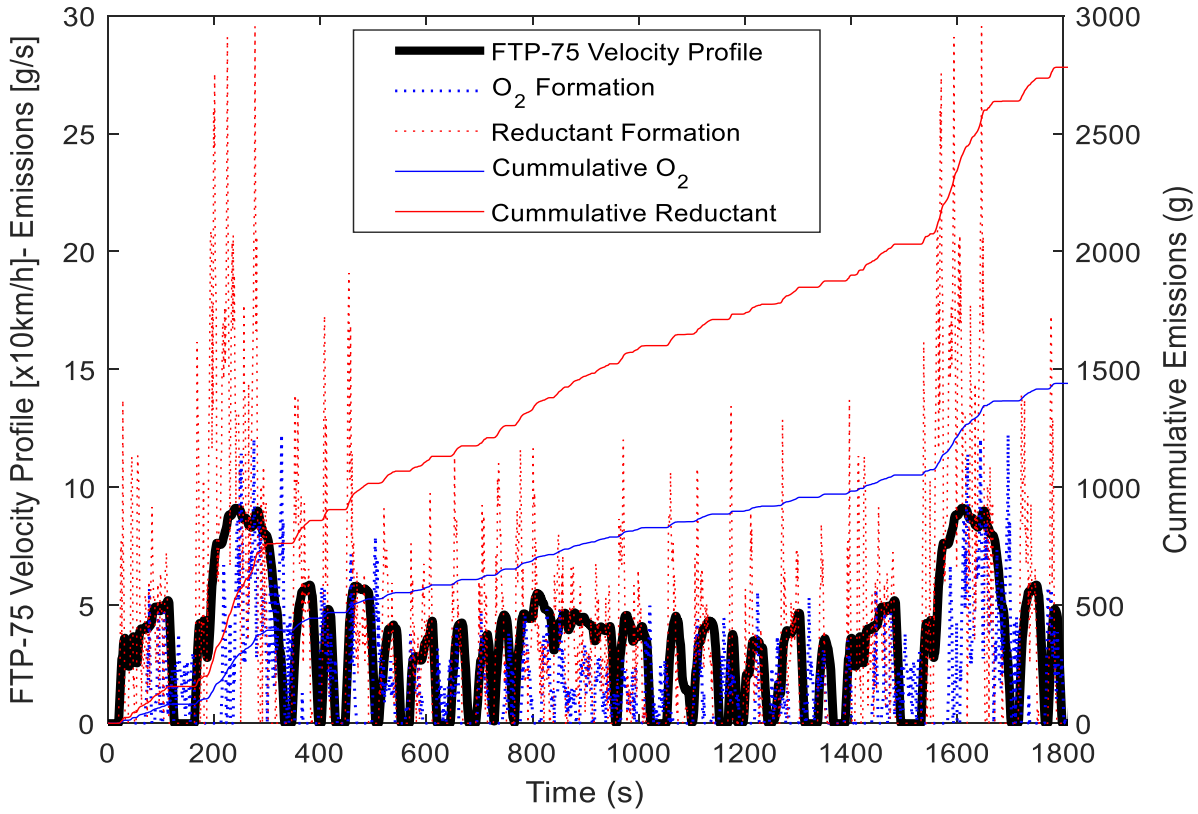

Figure 3-18 Lumped emissions formation during the FTP-75 Cycle using a simulated test vehicle

4. CONCLUSION AND FUTURE WORK

Engine and automotive research focus on improving fuel economy while maintaining emissions levels within the legal limits. The proposed models present an addition to the integrated systems simulation in the automotive field. The overall comprehensive model presents a virtual vehicle model, which can improve engine control and design parameters. The model offers a well-structured basis for TWC control and optimization. The lack of enough knowledge of the transient phases emphasizes the importance of the proposed model structure. The steady-state analysis has been intensely investigated at the laboratory and field-testing levels, encouraging the integrated tools and techniques to cover the gap during transient stages. The developed exhaust manifold model improves the prediction accuracy for upstream TWC exhaust gas parameters such as density, pressure, and velocity by around 5%. The accurate prediction improves the in-depth studies for TWC reactions and subsequently optimizes the operation through chemical reaction modeling and control-oriented modeling.

The accurate estimation of transient vehicle emissions is crucial to improving vehicle emission technologies. Integrating the vehicle models (Engine, Manifold, and TWC) with a torque-speed model provides a tool to estimate emissions during driving cycles and examine component dependencies. The presented modular structure uses individual models as building blocks to form the integrated model.

The proposed integrated model predicts transient emissions by varying the solution time step and adjusting fuel inputs for the combustion process. The exhaust manifold is based on conservation principles, solved numerically using the second-order

LW2; consequently, setting the relevant model boundary conditions ensures that the combustion process is connected with the downstream components. The TWC model reflects the transient prediction by considering the oxygen storage and release mechanisms corresponding to the engine's fuel status. The error for estimated emissions (NO, CO, CO_2, O_2) during the drive cycle is as low as 10%, consistent with the reported results. The model presents an integrated tool capable of predicting the main reactions within a TWC and the oxygen storage capacity.

The proposed methodology to estimate transient emissions illustrates a physics-based tool for quantifying road emissions from vehicles without incorporating correcting factors or emission fit data used in empirically-based models. The integrated model's modular presentation incorporates additional components such as LNT and silencers, providing an adjustable tool for quantifying tailpipe emissions at low cost and high reliability.

In conclusion, the theoretical model agrees with experimental validation for the presented range of operation 1,000 to 4,000 RPM. The variations between experimental and theoretical models are mainly due to insufficient data on spark timing, actual fuel composition, heating value, and exact molecular weight. The unknown properties were adapted from the literature while formulating the theoretical simulations. Acquiring these data would improve the model's prediction accuracy compared with experimental results and improve the emissions prediction from SI engines under actual operating conditions.

Engine mapping techniques decrease the gap of transient emissions formulation. Using an engine dynamometer for drive cycle verification decreases the need for expensive chassis dynamometers and field experiments with excessive time for sensors setup. The engine mapping method improves the versatility of testing through rapid improvements to the engine and ease of access to engine components compared with an actual vehicle. The engine mapping technique is implemented to provide the basis of in-depth studies for transient emission analysis as an accurate estimation for emission data.

Future work

The presented work focuses on obtaining a comprehensive model for simulating the emissions from a multi-cylinder SI engine. As presented in section 3, the agreement between the theoretical and experimental results validates the theoretical model assumptions and the structure used for modeling.

The current work utilizes the inlet manifold pressure to account for load changes; however, to increase the model usability, it is recommended to include a throttle model to account for load changes more accurately. The throttle model should account for mass airflow, the pressure at the intake manifold, and the eddy effect created by the intake manifold geometry. Similarly, for experimental investigation, a control scheme can be developed to control the throttle using the ratio between the throttle body diameters to the flow of the inlet manifold diameter. Based on the ratio of the diameters, the opening angle is determined. The controller will ensures that the throttle valve opening matches the prescribed cycle velocity-time profile by correcting for the velocity measurement error. Additionally, a fuel characterization will provide accurate information on the

heating value of fuel, flash point, density, and autoignition temperature. The availability of these specifications are essential for accurate model parameterization and incorporation with the details for the chemical heat of reaction.

The goal for the integrated engine and catalyst system is expected to improve fuel economy. In general, improvements could be achieved by implementing additional models such as the LNT, silencers, and HEGO sensor components.

The key approach of improving the fuel economy is to maintain the AFR of the engine at stoichiometric ratio, which is actively managed through the ECU and are represented by built-in fuel maps. Accurate integrated emissions models are essential for the engine estimating the AFR. Low-order models help in tackling the challenge of capturing the characteristics of the system without imposing a computational effort.

5. REFERENCES

[1] EPA, “Final Rule for Control of Air Pollution from Motor Vehicles: Tier 3 Motor Vehicle Emission and Fuel Standards,” 2018. https://www.epa.gov/regulations-emissions-vehicles-and-engines/final-rule-control-air-pollution-motor-vehicles-tier-3.

[2] K. R. Muske, J. C. P. Jones, and J. W. Howse, “A model-based approach to automotive three-way catalyst on-board monitoring,” *J. Process Control*, vol. 18, no. 2, pp. 163–172, 2008.

[3] EIA, “Monthly Energy Review,” 2018. https://www.eia.gov/totalenergy/data/monthly/.

[4] R. S. Benson, R. D. Garg, and D. Woollatt, “A numerical solution of unsteady flow problems,” *Int. J. Mech. Sci.*, vol. 6, no. 1, pp. 117–144, 1964.

[5] D. E. Winterbone, R. J. Pearson, M. S. Qatu, and S. Siavoshani, “Theory of engine manifold design: wave action methods for ic engineers,” *Appl. Mech. Rev.*, vol. 54, no. 6, pp. B109–B110, 2001.

[6] P. A. Lakshminarayanan, P. A. Janakiraman, M. K. G. Babu, and B. S. Murthy, “Prediction of gas exchange processes in a single cylinder internal combustion engine,” SAE Technical Paper, 1979.

[7] M. Takizawa, T. Uno, T. Oue, and T. Yura, “A study of gas exchange process simulation of an automotive multi-cylinder internal combustion engine,” *SAE Trans.*, pp. 1663–1676, 1982.

[8] S. Meisner and S. C. Sorenson, “Computer simulation of intake and exhaust manifold flow and heat transfer,” SAE Technical Paper, 1986.

[9] M. Chapman, “FRAM—Nonlinear damping algorithms for the continuity equation,” *J. Comput. Phys.*, vol. 44, no. 1, pp. 84–103, 1981.

[10] T. Morel, J. Morel, and D. A. Blaser, “Fluid dynamic and acoustic modeling of

concentric-tube resonators/silencers," *SAE Trans.*, pp. 35–51, 1991.

[11] B. Peters and A. D. Gosman, "Numerical simulation of unsteady flow in engine intake manifolds," SAE Technical Paper, 1993.

[12] Y. H. Zahran, "A class of high order TVD schemes for systems of conservation laws," *Port. Math.*, vol. 64, no. 2, pp. 155–174, 2007.

[13] A. Onorati, G. Ferrari, and G. D'Errico, "Fluid Dynamic Modeling of the Gas Flow with Chemical Specie Transport through the Exhaust Manifold of a Four Cylinder SI Engine," *SAE Trans.*, vol. 108, pp. 819–834, Apr. 1999, [Online]. Available: http://www.jstor.org/stable/44743416.

[14] Z. Gao, J. C. Conklin, C. S. Daw, and V. K. Chakravarthy, "A proposed methodology for estimating transient engine-out temperature and emissions from steady-state maps," *Int. J. Engine Res.*, vol. 11, no. 2, pp. 137–151, Feb. 2010, doi: 10.1243/14680874JER05609.

[15] S. J. Kirkpatrick, G. P. Blair, R. Fleck, and R. K. McMullan, "Experimental Evaluation of 1-D Computer Codes for the Simulation of Unsteady Gas Flow Through Engines - A First Phase," *SAE Trans.*, vol. 103, pp. 1711–1730, Apr. 1994, [Online]. Available: http://www.jstor.org/stable/44632907.

[16] T. Morel and M. F. Flemming, "Characterization of manifold dynamics in the Chrysler 2.2 SI engine by measurements and simulation," SAE Technical Paper, 1990.

[17] A. Onorati, G. Ferrari, G. Montenegro, A. Caraceni, and P. Pallotti, "Prediction of SI engine emissions during an ECE driving cycle via integrated thermo-fluid dynamic simulation," SAE Technical Paper, 2004.

[18] G. Q. Zhang and D. N. Assanis, "Manifold gas dynamics modeling and its coupling with single-cylinder engine models using Simulink," *J. Eng. Gas Turbines Power*, vol. 125, no. 2, pp. 563–571, 2003.

[19] Q. Zhang, A. Pennycott, R. Burke, S. Akehurst, and C. Brace, “Predicting the nitrogen oxides emissions of a diesel engine using neural networks,” SAE Technical Paper, 2015.

[20] G. D’Errico, G. Ferrari, A. Onorati, and T. Cerri, “Modeling the pollutant emissions from a SI engine,” *SAE Trans.*, pp. 1–11, 2002.

[21] R. S. Benson, W. J. D. Annand, and P. C. Baruah, “A simulation model including intake and exhaust systems for a single cylinder four-stroke cycle spark ignition engine,” *Int. J. Mech. Sci.*, vol. 17, no. 2, pp. 97–124, 1975.

[22] J. H. Horlock and D. E. Winterbone, “The thermodynamics and gas dynamics of internal-combustion engines. Volume II,” 1986.

[23] D. K. S. Chen, “A numerical model for thermal problems in exhaust systems,” SAE Technical Paper, 1993.

[24] S. K. S. Korremla, “Experimental investigation of steady state heat transfer phenomenon in Pontiac G6 vehicle exhaust system,” The University of Texas at El Paso, 2007.

[25] V. Gnielinski, “Turbulent heat transfer in annular spaces—a new comprehensive correlation,” *Heat Transf. Eng.*, vol. 36, no. 9, pp. 787–789, 2015.

[26] J. P. Abraham, E. M. Sparrow, and J. C. K. Tong, “Heat transfer in all pipe flow regimes: laminar, transitional/intermittent, and turbulent,” *Int. J. Heat Mass Transf.*, vol. 52, no. 3–4, pp. 557–563, 2009.

[27] H. Hausen, “Heat transfer in counterflow, parallel-flow, and cross-flow,” 1983.

[28] R. M. Frank, “A computer model for the heat losses in the exhaust manifold of an internal combustion engine.” Massachusetts Institute of Technology, 1986.

[29] G. Fiengo, J. W. Grizzle, J. A. Cook, and A. Y. Karnik, “Dual-UEGO active catalyst control for emissions reduction: Design and experimental validation,” *IEEE Trans. Control Syst. Technol.*, vol. 13, no. 5, pp. 722–736, 2005.

[30] E. G. Giakoumis and G. Triantafillou, “Analysis of the Effect of Vehicle, Driving and Road Parameters on the Transient Performance and Emissions of a Turbocharged Truck,” *Energies* , vol. 11, no. 2. 2018, doi: 10.3390/en11020295.

[31] E. P. Brandt, Y. Wang, and J. W. Grizzle, “Dynamic modeling of a three-way catalyst for SI engine exhaust emission control,” *IEEE Trans. Control Syst. Technol.*, vol. 8, no. 5, pp. 767–776, 2000.

[32] K. Kuklinska, L. Wolska, and J. Namiesnik, “Air quality policy in the US and the EU–a review,” *Atmos. Pollut. Res.*, vol. 6, no. 1, pp. 129–137, 2015.

[33] H.-M. Streib and H. Bischof, “Electronic throttle control (ETC): A cost effective system for improved emissions, fuel economy, and driveability,” SAE Technical Paper, 1996.

[34] L. Lan *et al.*, “Promotion of CeO2–ZrO2–Al2O3 composite by selective doping with barium and its supported Pd-only three-way catalyst,” *J. Mol. Catal. A Chem.*, vol. 410, pp. 100–109, 2015.

[35] S. E. Voltz, C. R. Morgan, D. Liederman, and S. M. Jacob, “Kinetic Study of Carbon Monoxide and Propylene Oxidation on Platinum Catalysts,” *Prod. R&D*, vol. 12, no. 4, pp. 294–301, Dec. 1973, doi: 10.1021/i360048a006.

[36] R. E. Hayes, L. S. Mukadi, M. Votsmeier, and J. Gieshoff, “Three-way catalytic converter modelling with detailed kinetics and washcoat diffusion,” *Top. Catal.*, vol. 30, no. 1, pp. 411–415, 2004.

[37] S. Siemund, J. P. Leclerc, D. Schweich, M. Prigent, and F. Castagna, “Three-way monolithic converter: Simulations versus experiments,” *Chem. Eng. Sci.*, vol. 51, no. 15, pp. 3709–3720, 1996, doi: https://doi.org/10.1016/0009-2509(96)00018-8.

[38] C. Dubien, D. Schweich, G. Mabilon, B. Martin, and M. Prigent, “Three-way catalytic converter modelling: fast- and slow-oxidizing hydrocarbons, inhibiting species, and

steam-reforming reaction," *Chem. Eng. Sci.*, vol. 53, no. 3, pp. 471–481, 1998, doi: https://doi.org/10.1016/S0009-2509(97)00313-8.

[39] C. Depcik, D. Assanis, and K. Bevan, "A one-dimensional lean NO x trap model with a global kinetic mechanism that includes NH3 and N2O," *Int. J. Engine Res.*, vol. 9, no. 1, pp. 57–77, 2008.

[40] K. Ramanathan and C. S. Sharma, "Kinetic parameters estimation for three way catalyst modeling," *Ind. Eng. Chem. Res.*, vol. 50, no. 17, pp. 9960–9979, 2011.

[41] P. Kumar, I. Makki, J. Kerns, K. Grigoriadis, M. Franchek, and V. Balakotaiah, "A low-dimensional model for describing the oxygen storage capacity and transient behavior of a three-way catalytic converter," *Chem. Eng. Sci.*, vol. 73, pp. 373–387, 2012, doi: https://doi.org/10.1016/j.ces.2011.12.001.

[42] J. B. Heywood, *Internal combustion engine fundamentals*. McGraw-Hill Education, 2018.

[43] M. GRIFFIN, R. Diwakar, J. R. ANDERSON J, and E. Jones, "Computational fluid dynamics applied to flows in an internal combustion engine," in *16th Aerospace Sciences Meeting*, 1978, p. 57.

[44] N. Dinler and N. Yucel, "Numerical simulation of flow and combustion in an axisymmetric internal combustion engine," in *Proceedings of World Academy of Science, Engineering and Technology*, 2007, vol. 22.

[45] T. Schmiedl and U. Seifert, "Efficiency at maximum power: An analytically solvable model for stochastic heat engines," *EPL (Europhysics Lett.*, vol. 81, no. 2, p. 20003, 2007.

[46] E. Hendricks and S. C. Sorenson, "Mean value modelling of spark ignition engines," *SAE Trans.*, pp. 1359–1373, 1990.

[47] C. N. Pratheeba and P. Aghalayam, “Effect of exhaust gas recirculation in NOx control for compression ignition and homogeneous charge compression ignition engines,” *Energy Procedia*, vol. 66, pp. 25–28, 2015.

[48] B. Ashok, S. D. Ashok, and C. R. Kumar, “A review on control system architecture of a SI engine management system,” *Annu. Rev. Control*, vol. 41, pp. 94–118, 2016.

[49] M. Bhattacharya, M. P. Harold, and V. Balakotaiah, “Low-dimensional models for homogeneous stirred tank reactors,” *Chem. Eng. Sci.*, vol. 59, no. 22, pp. 5587–5596, 2004, doi: https://doi.org/10.1016/j.ces.2004.07.068.

[50] H. J. Curran, P. Gaffuri, W. J. Pitz, and C. K. Westbrook, “A comprehensive modeling study of iso-octane oxidation,” *Combust. Flame*, vol. 129, no. 3, pp. 253–280, 2002, doi: https://doi.org/10.1016/S0010-2180(01)00373-X.

[51] N. M. Marinov, C. Westbrook, and W. J. Pitz, “Detailed and global chemical kinetics model for hydrogen,” 1995.

[52] P. Kumar, M. Franchek, K. Grigoriadis, and V. Balakotaiah, “Fundamentals-based low-dimensional combustion modeling of spark-ignited internal combustion engines,” *AIChE J.*, vol. 57, no. 9, pp. 2472–2492, 2011.

[53] W. P. Jones and R. P. Lindstedt, “Global reaction schemes for hydrocarbon combustion,” *Combust. Flame*, vol. 73, no. 3, pp. 233–249, 1988, doi: https://doi.org/10.1016/0010-2180(88)90021-1.

[54] S. Berglund, “A model of turbocharged engines as dynamic drivetrain members,” *SAE Trans.*, pp. 1027–1034, 1993.

[55] C. I. Rackmil, P. N. Blumberg, D. A. Becker, R. R. Schuller, and D. C. Garvey, “A dynamic model of a locomotive diesel engine and electrohydraulic governor,” 1988.

[56] Q. Jiang, “Prediction of diesel engine particulate emission during transient cycles.” Iowa

State University, 1991.

[57] C. Ericson, B. Westerberg, and R. Egnell, “Transient emission predictions with quasi stationary models,” SAE Technical Paper, 2005.

[58] E. G. Giakoumis and S. C. Lioutas, “Diesel-engined vehicle nitric oxide and soot emissions during the European light-duty driving cycle using a transient mapping approach,” *Transp. Res. Part D Transp. Environ.*, vol. 15, no. 3, pp. 134–143, 2010, doi: https://doi.org/10.1016/j.trd.2009.12.003.

[59] J. R. Hagena, Z. Filipi, and D. N. Assanis, “Transient diesel emissions: analysis of engine operation during a tip-in,” SAE Technical Paper, 2006.

[60] S. Roy, R. Banerjee, and P. K. Bose, “Performance and exhaust emissions prediction of a CRDI assisted single cylinder diesel engine coupled with EGR using artificial neural network,” *Appl. Energy*, vol. 119, pp. 330–340, 2014.

[61] P. Kirchen, P. Obrecht, and K. Boulouchos, “Soot emission measurements and validation of a mean value soot model for common-rail diesel engines during transient operation,” *SAE Int. J. engines*, vol. 2, no. 1, pp. 1663–1678, 2009.

[62] E. G. Giakoumis, *Driving and engine cycles*, vol. 1. Springer, 2017.

[63] E. G. Giakoumis and A. T. Zachiotis, “Investigation of a Diesel-Engined Vehicle’s Performance and Emissions during the WLTC Driving Cycle—Comparison with the NEDC,” *Energies* , vol. 10, no. 2. 2017, doi: 10.3390/en10020240.

[64] M. Honek, S. Wojnar, P. Simoncic, and B. Rohar-Hkiv, “Control of electronic throttle valve position of SI engine,” in *International Conference February*, 2010, vol. 10, p. 13.

[65] A. S. van Niekerk, P. J. Kay, B. Drew, and N. Larsen, “Optimisation of low temperature combustion technology, for future drive cycles, using a factorial design of experiments,” SAE Technical Paper, 2019.

[66] D. Bergman, “Quantification of Drive Cycles for Evaluating Motor Efficiency.” 2021.

[67] P. Fernandes, E. Macedo, B. Bahmankhah, R. F. Tomas, J. M. Bandeira, and M. C. Coelho, “Are internally observable vehicle data good predictors of vehicle emissions?,” *Transp. Res. Part D Transp. Environ.*, vol. 77, pp. 252–270, 2019.

[68] A. A. Kolin, S. E. Silantyev, and P. S. Rogov, “Ways to reduce fuel consumption of a light commercial vehicle for WLTC and NEDC cycles,” in *IOP Conference Series: Materials Science and Engineering*, 2021, vol. 1086, no. 1, p. 12039.

[69] J. L. Jiménez, J. Valido, and N. Molden, “The drivers behind differences between official and actual vehicle efficiency and CO2 emissions,” *Transp. Res. Part D Transp. Environ.*, vol. 67, pp. 628–641, 2019.

[70] J. Fu *et al.*, “Application of artificial neural network to forecast engine performance and emissions of a spark ignition engine,” *Appl. Therm. Eng.*, vol. 201, p. 117749, 2022.

[71] J. Liu, Q. Huang, C. Ulishney, and C. E. Dumitrescu, “Comparison of Random Forest and Neural Network in Modeling the Performance and Emissions of a Natural Gas Spark Ignition Engine,” *J. Energy Resour. Technol.*, vol. 144, no. 3, 2022.

[72] Q. Huang, J. Liu, C. Ulishney, and C. E. Dumitrescu, “On the use of artificial neural networks to model the performance and emissions of a heavy-duty natural gas spark ignition engine,” *Int. J. Engine Res.*, p. 14680874211034408, 2021.

[73] S. Brusca, R. Lanzafame, and M. Messina, “Neural Network application to evaluate thermodynamic properties of ICE’s combustion gases,” in *SAE 2005 World Congress & Exhibition*, 2005, no. 2005-01–1128.

[74] S. Esposito, M. Mally, L. Cai, H. Pitsch, and S. Pischinger, “Validation of a RANS 3D-CFD gaseous emission model with space-, species-, and cycle-resolved measurements from an SI DI engine,” *Energies*, vol. 13, no. 17, p. 4287, 2020.

[75] R. Ortiz-Imedio, A. Ortiz, and I. Ortiz, “Comprehensive analysis of the combustion of low carbon fuels (hydrogen, methane and coke oven gas) in a spark ignition engine through CFD modeling,” *Energy Convers. Manag.*, vol. 251, p. 114918, 2022.

[76] M. Mirzaeian and S. Langridge, “Creating a Virtual Test Bed Using a Dynamic Engine Model with Integrated Controls to Support in-the-Loop Hardware and Software Optimization and Calibration,” *Energies*, vol. 14, no. 3, p. 652, 2021.

[77] K. Bajpai, A. Chandrakar, A. Agrawal, and S. Shekhar, “CFD analysis of exhaust manifold of SI engine and comparison of back pressure using alternative fuels,” *IOSR J. Mech. Civ. Eng.*, vol. 14, no. 1, pp. 23–29, 2017.

[78] O. Holmer and L. Eriksson, “A Mean Value Model for Unsteady Gas Flows and Heat Transfer in Pipes,” in *Proceedings of The 59th Conference on Simulation and Modelling (SIMS 59), 26-28 September 2018, Oslo Metropolitan University, Norway*, 2018, no. 153, pp. 284–289.

[79] S. Doulgeris, A. Dimaratos, N. Zacharof, Z. Toumasatos, D. Kolokotronis, and Z. Samaras, “Real world fuel consumption prediction via a combined experimental and modeling technique,” *Sci. Total Environ.*, vol. 734, p. 139254, 2020.

[80] S. Le Guen, A. Maiboom, S. Bougrine, and X. Tauzia, “Analysis of systematic calibration of heat transfer models on a turbocharged GDI engine operating map,” SAE Technical Paper, 2018.

[81] R. Tatschl *et al.*, “Virtual Component and System Integration for Efficient Electrified Vehicle Development,” *Proc. 8th Transp. Res. Arena TRA*, pp. 27–30, 2020.

[82] G. Montenegro *et al.*, “Prediction of Driving Cycles by Means of a Co-Simulation Framework for the Evaluation of IC Engine Tailpipe Emissions,” SAE Technical Paper, 2020.

[83] T. Cerri *et al.*, “A Novel 1D Co-Simulation Framework for the prediction of Tailpipe Emissions under different IC engine operating conditions,” SAE Technical Paper, 2019.

[84] A. Onorati, G. Ferrari, and G. D’Errico, “1D unsteady flows with chemical reactions in the exhaust duct-system of SI engines: predictions and experiments,” *SAE Trans.*, pp. 738–752, 2001.

[85] M. Kushwahu, “16 - Tribological issues in cam–tappet contacts,” H. B. T.-T. and D. of E. and P. Rahnejat, Ed. Woodhead Publishing, 2010, pp. 545–566.

[86] A. Olczyk, “Identification of dynamic phenomena in pipes supplied with a pulsating flow of gas,” *Proc. Inst. Mech. Eng. Part C J. Mech. Eng. Sci.*, vol. 223, no. 8, pp. 1851–1867, 2009.

[87] T. Markel *et al.*, “ADVISOR: a systems analysis tool for advanced vehicle modeling,” *J. Power Sources*, vol. 110, no. 2, pp. 255–266, 2002, doi: https://doi.org/10.1016/S0378-7753(02)00189-1.